

## Article

# Geochemical and Geochronological Constraints of Permian-Triassic Magmatism on Oceanic Subduction and Continental Collision during the Eastern Paleo-Tethyan Evolution

Wentao Xu <sup>1</sup>, Fulai Liu <sup>1,\*</sup>, Wang Xu <sup>1</sup>, Huining Wang <sup>1</sup>, Lei Ji <sup>2</sup>, Fang Wang <sup>1</sup> and Dan Wang <sup>1</sup>

<sup>1</sup> Key Laboratory of Deep-Earth Dynamics of Ministry of Natural Resources, Institute of Geology, Chinese Academy of Geological Sciences, Beijing 100037, China; xuwentao@163.com (W.X.); wangxu\_k@126.com (W.X.); wanghuining1@126.com (H.W.); wangfang\_mr@163.com (F.W.); wangd221@gmail.com (D.W.)

<sup>2</sup> State Key Laboratory of Geological Processes and Mineral Resources, Chinese Academy of Geological Sciences, Beijing 100037, China; jileicags@126.com

\* Correspondence: lfl0225@sina.com

**Abstract:** The Jinshajiang–Ailaoshan–Song Ma orogenic belt (JASB), as a vital segment of the eastern Paleo-Tethyan tectonic zone, is one of the most important zones in which to study the Paleo-Tethyan tectonic evolution. We have undertaken an integrated geochronological, petrological, and geochemical study of mafic rocks from the JASB to reveal the subduction and closure processes of the eastern Paleo-Tethyan Ocean during the Permian to Triassic. In conjunction with previous magmatic and metamorphic records in the JASB, three important tectonic stages are identified: (1) Early Permian to Early Triassic (ca. 288–248 Ma). Most of the Early Permian to Early Triassic mafic rocks have normal mid-ocean ridge basalt (N-MORB)- or enriched MORB (E-MORB)-like rare earth elements (REE) and trace element-normalized patterns with positive  $\epsilon\text{Nd}(t)$  and  $\epsilon\text{Hf}(t)$  values and negative Nb and Ta anomalies. Their La/Nb ratios and  $\epsilon\text{Nd}(t)$  values show that approximately 3%–15% of slab-derived fluid accounts for the generation of these rocks. These characteristics suggest that the mafic rocks formed in an arc/back-arc basin setting at this stage. Additionally, the Early Permian mafic rocks are mainly exposed in the Jomda–Weixi–Yaxuanqiao–Truong Son magmatic rock belt (JYTB) on the western side of the JASB, indicating that the westward subduction of the Jinshajiang–Ailaoshan–Song Ma Paleo-Tethys Ocean (JASO) began in the Early Permian. Middle Permian mafic rocks are exposed in the Ailaoshan–Day Nui Con Voi metamorphic complex belt and the JYTB on both sides of the JASB. We propose that the bipolar subduction of the JASO occurred in the Middle Permian and ended in the Early Triassic. (2) Middle Triassic (ca. 248–237 Ma). The mafic rocks at this stage have LREE- and LILE-enriched patterns, negative Nb and Ta anomalies and negative  $\epsilon\text{Nd}(t)$  values. Their variable  $\epsilon\text{Hf}(t)$ ,  $\epsilon\text{Nd}(t)$  values and La/Nb ratios show that these mafic rocks were highly affected by crustal material (ca. 16%). Considering the Middle Triassic high-pressure (HP) metamorphism and massive Al-enriched felsic magmatism in the JASB, these rocks may have formed in a collisional setting between the South China Block (SCB) and the North Qiangtang–Simao–Indochina Block (QSIB) during the Middle Triassic. (3) Late Triassic (ca. 235–202 Ma). The mafic rocks at this stage have negative  $\epsilon\text{Nd}(t)$  and  $\epsilon\text{Hf}(t)$  values and show terrestrial array characteristics. The  $\epsilon\text{Nd}(t)$  values and La/Nb ratios show that approximately 30% of crustal components account for the generation of these rocks. Combined with the contemporaneous bimodal magma and metamorphism during the Late Triassic, we suggest that these rocks may have formed in a postcollisional extensional setting associated with magma diapir.

**Keywords:** eastern Paleo-Tethys; Jinshajiang–Ailaoshan–Song Ma orogenic belt; mafic rocks; Permian to Triassic; tectonic evolution



**Citation:** Xu, W.; Liu, F.; Xu, W.; Wang, H.; Ji, L.; Wang, F.; Wang, D. Geochemical and Geochronological Constraints of Permian-Triassic Magmatism on Oceanic Subduction and Continental Collision during the Eastern Paleo-Tethyan Evolution. *Minerals* **2022**, *12*, 633. <https://doi.org/10.3390/min12050633>

Academic Editors: Simon Paul Johnson, Fuhao Xiong and Lin Hou

Received: 14 April 2022

Accepted: 13 May 2022

Published: 17 May 2022

**Publisher's Note:** MDPI stays neutral with regard to jurisdictional claims in published maps and institutional affiliations.



**Copyright:** © 2022 by the authors. Licensee MDPI, Basel, Switzerland. This article is an open access article distributed under the terms and conditions of the Creative Commons Attribution (CC BY) license (<https://creativecommons.org/licenses/by/4.0/>).

## 1. Introduction

The Jinshajiang–Ailaoshan–Song Ma orogenic belt (JASB) is located in southwestern China and constitutes an essential part of the expansive Tethyan–Himalayan domain as a consecutive Paleo-Tethyan orogenic belt [1–4]. However, the JASB has a complicated history of tectonic evolution prior to the final collision between the South China Block (SCB) and the North Qiangtang–Simao–Indochina Block (QSIB; e.g., [5–10]). How and when the Jinshajiang–Ailaoshan–Song Ma Paleo-Tethyan Ocean (JASO) opened, subducted, and closed has confused researchers due to a lack of comprehensive studies of the geochronology and petrogenesis of magmatism in the JASB [11–14].

The different stages of the tectonic cycle, or the Wilson cycle [15], are always accompanied by various mafic rock types [16]. These mafic rocks with distinctive geochemical fingerprints can reveal their specific tectonic settings [17,18]. Based on the studies of Ordovician to Silurian WPB-like mafic rocks in the JASB, Liu et al. [11] and Jian et al. [19] proposed that the SCB may have begun to separate from Gondwana in response to the Late Ordovician–Silurian Proto-Tethyan subduction. Geochronological and geochemical studies of Paleo-Tethys related ophiolites in the JASB suggested that the JASO was a small and slow-spreading oceanic basin during the Late Devonian to Late Carboniferous (e.g., [5,19–23]). In addition, the abundance of Permian to Triassic mafic-felsic rocks (e.g., [24–32]) and metamorphic rocks (e.g., [33–36]) in the JASB is considered to be compelling evidence for the reconstruction of the subduction and closure processes of the JASO.

In this study, we report on Permian to Triassic mafic rocks, and present a synthesis of the magmatic and metamorphic records associated with the Permian to Triassic evolution of the JASB. This research provides robust constraints on the ages, nature, and genesis of these rocks, which enable us to better understand their geodynamic setting and tectonic implications in the context of Paleo-Tethyan subduction and collisional history.

## 2. Regional Geology

The JASB is located in the southeastern Tibetan Plateau, extending WNW–ESE across the northern Tibetan Plateau to NNW–SSE across the southeastern Tibetan Plateau over more than 2000 km (Figure 1a). The eastern and western sides of the JASB comprise the SCB and the QSIB, respectively (Figure 1b). The JASB consists of the Jinshajiang–Ailaoshan–Song Ma suture (JASS), Jomda–Weixi–Yaxuanqiao–Truong Son volcanic arc (JYTA) and a number of metamorphic complex belts, including the Xuelongshan, Diancangshan, Ailaoshan, Day Nui Con Voi, and Song Ma belts [10,33,37–44].

### 2.1. The Jinshajiang–Ailaoshan–Song Ma Suture Belt

The Jinshajiang suture and the Ailaoshan suture to the southeast are thought to be contiguous and are also believed to align with the Song Ma suture farther south in Vietnam and the Bangxi–Chenxing orogenic belt on Hainan Island [2,45–47]. The suture zones are defined by a discontinuous belt of ophiolite fragments and mélangé, and are inferred to represent remnants of a back-arc basin or a branch of the Paleo-Tethyan Ocean [5,19,22,48–51]. The ophiolite mélangés consist of dismembered serpentinized peridotites and are layered mafic-ultramafic rocks, sheeted dikes, MORB-like lavas and radiolarian-bearing cherts, and are intercalated with exotic limestone fragments [52]. The gabbros, dolerites, plagiogranites, and anorthosites from these ophiolite mélangés yield zircon U–Pb ages of 383–304 Ma [5,7,19,22,49,53–55]. Among these three suture belts, the location of the Ailaoshan suture belt has long been the most debated. Xia et al. [56] and Xu et al. [13] proposed that the Ailaoshan suture may lie along or in close proximity to the Ailaoshan–Tengtiaohe fault. However, some researchers support that the Jiujiia–Anding fault [57] or the Amojiang–Lixianjiang fault [37] may be the boundaries of the Simao–Indochina Block and SCB. Additionally, the detrital zircon U–Pb ages and Hf isotope data of the Cambrian–Devonian sedimentary units in the Ailaoshan belt and its adjacent western margin of the SCB indicate distinctive detrital zircon provenance variations on the different sides of the Ailaoshan suture [56,58]. Subsequently, a distinct change in the detrital provenance and

depositional setting is present across the Middle–Late Triassic boundary [13], and the Late Triassic molasses sequences overlap units of the Jiapila and Yiwanshui formations, unconformably overlying the metamorphic rocks in the Jinshajiang–Ailaoshan suture belt, which indicates closure of the Jinshajiang–Ailaoshan ocean [22].

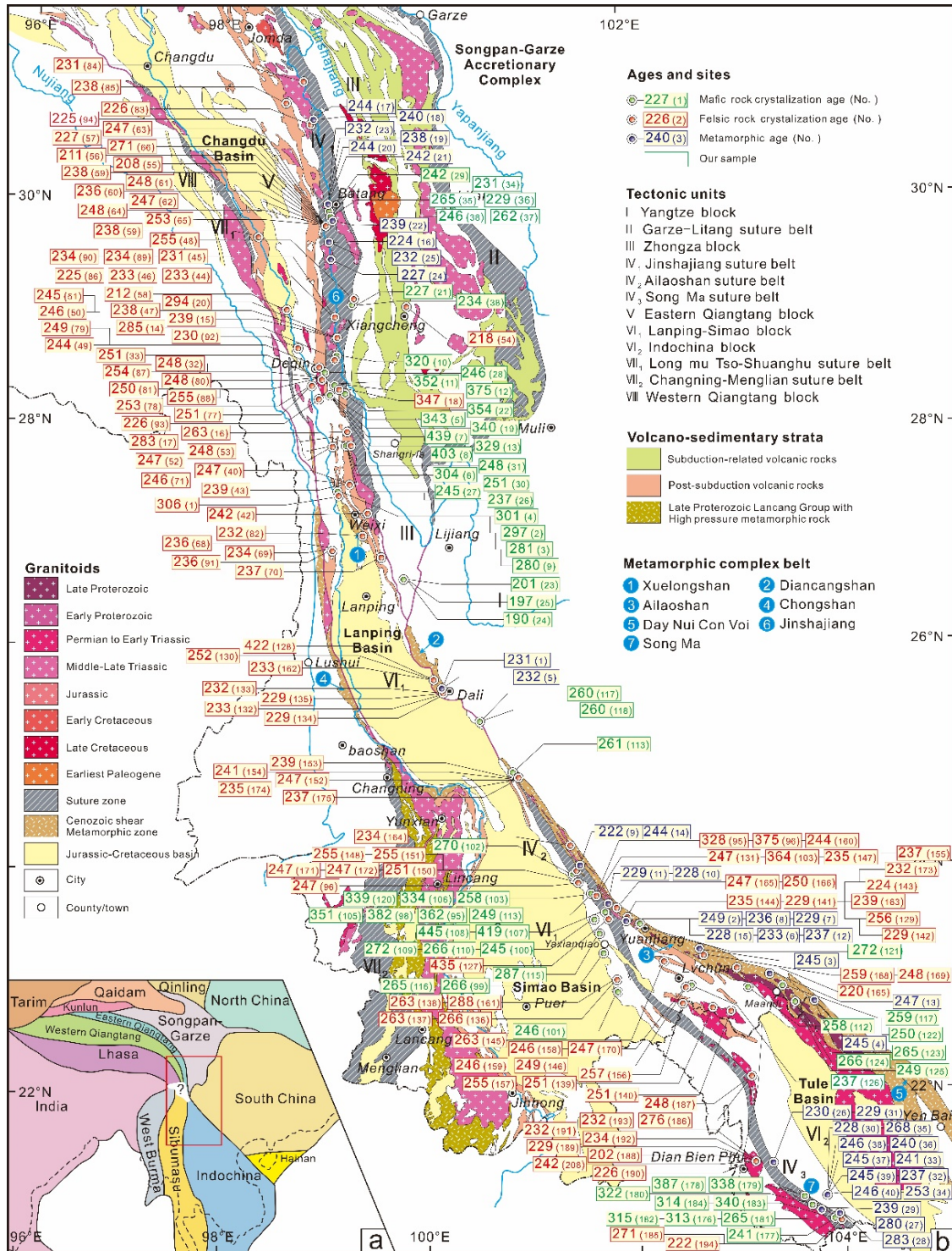


**Figure 1.** (a) Tectonic framework of the southwestern Tibet region; (b) Simplified geological map showing the major continental Blocks, suture belts, and the distribution of Ordovician-Triassic magmatic and metamorphic rocks, as well as the location of crystallization and metamorphic ages in the JASB. Revised from Deng et al. [38].

## 2.2. The Jomda–Weixi–Yaxuanqiao–Truong Son Volcanic Arc

The Jomda–Weixi volcanic arc on the eastern margin of the Qiangtang–Simao Block (Figure 1b) consists of Permian to Early Triassic tholeiitic, calc-alkaline, and shoshonitic volcanic rocks and Late Triassic intracontinental volcanic rocks, including rhyolite, dacite, andesite, and calc-alkaline basalt, in the inner part of the Block [43,44,59]. This arc belt is diachronous, with younger igneous rocks along its southern part than along its northwestern part [43]. The occurrence of the arc setting was argued to have been generated by westward subduction of the Jinshajiang oceanic crust along with determining ages [59,60]. The extensional rift was superposed on the Jomda–Weixi volcanic arc and filled by Late-Triassic bimodal volcanic rocks and microclastic and turbidite sequences from north to south [59].

The Yaxuanqiao volcanic arc lies on the eastern margin of the Simao terrane and parallel to the Ailaoshan ophiolite belt (Figure 1b). This arc consists of a suite of calc-alkaline lavas (basalt, andesite and dacite), intrusions (gabbro, dolerite and plagioclase pyroxenite) and sandy to shaly sediments [51]. The intrusive rocks are intruded or covered by basalt. Fan et al. [48], Jian et al. [19], Lai et al. [24], and Liu et al. [61] obtained Early Permian to Middle Triassic ages (288–245 Ma) of these intrusions, which were probably related to intracontinental subduction on the eastern margin of the Simao terrane.

The Truong Song volcanic arc is a NW–SE oriented volcanic belt lying on the eastern margin of the Indochina terrane and west of the Song Ma suture belt (Figure 1b). There are three plutonic complexes along the Truong Son volcanic arc, including the Chieng Khuong, Dien Bien and Song Ma complexes. Within the belt, Early Permian to Late Triassic (ca. 281–201 Ma) plutonic intrusions are widespread along the Truong Son volcanic arc. Early Permian to Early Triassic (288–245 Ma) arc magmatism presents reliable information on the subduction of the Song Ma oceanic plate [39,62–65], whereas Late Triassic magmatism (229–202 Ma) was formed during postcollisional extension along the Song Ma orogenic belt [39,66].

## 2.3. The Jinshajiang–Ailaoshan–Song Ma Metamorphic Complex Belt

The metamorphic rocks that crop out discontinuously along the Xuelongshan, Diancangshan and Ailaoshan ranges represent a Precambrian crystalline basement (Figure 1b; [51,67]) and contain migmatites that yield zircon U–Pb ages of ca. 843–833 Ma [68]. These ages are similar to those from the Yangtze Block basement [51]. The Jinshajiang metamorphic complex belt (JMB) lies on the northeastern Xuelongshan metamorphic complex belt (XMB; Figure 1b). The JMB, passing through Baiyu, Batang, Derong, Benzilan, and Zhongdian to Yunnan Province (ca. 300 km), is bounded by the Yushu–Yangla Bending fault and Oubana–Dingquhe–Zhongdian fault on the eastern and western sides (ca. 40 km), respectively [69]. The metamorphic rocks exposed along the JMB exhibit a gradient from chlorite grade to biotite, garnet, staurolite-kyanite, and sillimanite grades from east to west [22,70]. These rocks are mainly metapelites, amphibolites, and marbles, ranging in grade from greenschist to high amphibolite facies [22]. In the northern part of the JMB, Tang et al. [36] recently found ultrahigh-pressure (UHP) retrograde eclogite in the Luomai and Gonjo areas and garnet-bearing blueschist and eclogite in the Qiangtang area, central Tibet [71]. The metamorphic ages are limited to between 244 and 224 Ma by zircon U–Pb dating of eclogite and white mica  $^{40}\text{Ar}/^{39}\text{Ar}$  dating of garnet schist, and represent the westward subduction–collision epoch of the Paleo-Tethyan Ocean located between the Yangtze Block and Qiangtang–Simao Block [36,70].

The Diancangshan–Ailaoshan metamorphic complex belt (DAMB) presents as a NW–SE oriented unit that extends over 1000 km on the western margin of the SCB (Figure 1b; [72,73]). There are two principal ridges, e.g., a ca. 60 km-long ridge to the northwest of Dali (Diancangshan) and a 500 km-long ridge to the southeast (Ailaoshan). Both of these areas can be subdivided into high-grade and low-grade metamorphic belts. This complex belt contains paragneisses and orthogneisses with lenses and Blocks of

amphibolites and garnet pyroxenites, thin layers of kyanite- and mica-bearing schists, and younger leucogranite layers, migmatites, and dikes [33,74]. HP metamorphic zircons from paragneisses, amphibolite, and garnet pyroxenites yield weighted  $^{206}\text{Pb}/^{238}\text{U}$  ages of 249–230 Ma, which reveal an HP metamorphic event in the Diancangshan–Ailaoshan complex during the Early–Middle Triassic [33]. However, metamorphic zircons from the garnet-bearing plagioclase two-mica schist in the Ailaoshan complex yield a weighted  $^{206}\text{Pb}/^{238}\text{U}$  age of  $222.3 \pm 1.2$  Ma, which is also regarded as evidence of the Paleo-Tethyan closure during the Middle–Late Triassic [34,75].

Permian–Triassic metamorphism is widely found along the Song Ma belt, Truong Son belt, and Kontum Massif of Vietnam [76,77]. The Song Ma belt in northern Vietnam consists of ophiolite, metamafic-ultramafic rocks, metasedimentary rocks, and eclogite. Triassic HP eclogites (ca. 230 Ma) are found in the northwestern Nam Co complex, northeast of Dian Bien Phu [6,78]. On the other hand, the monazite and zircon U–Pb tests of the polytic gneiss and garnet hornblende rock give weighted ages of 243 Ma to 228 Ma [6,55]. This medium-pressure (MP)–HP metamorphism is thought to have occurred during the closure stage of the Paleo-Tethyan Ocean.

### 3. Petrography and *P-T* Estimates

Mafic and metamafic samples were collected from the Batang area in the Jinshajiang orogenic belt and the Lvchun, Yaxuanqiao, Yuanjiang, and Maandi areas in the Ailaoshan orogenic belt to investigate the tectonic evolution of the JASB (Figure 1b). Mafic rock samples (e.g., basalt and gabbro samples: 17HA21-1, 18J18-1, 18J24-1, 18J28-1, and 18J33-1) collected from the Yaxuanqiao and Lvchun areas crop out in pillow (Figure 2f), massive or layered shapes (Figure 2g,h). Metamafic rocks are amphibolites or Grt-amphibolites from the Batang, Yuanjiang, and Maandi areas. Most amphibolites are sporadically distributed as thick layers or irregular blocks in gneisses or schists throughout the JMB and DAMB (Figure 2a–e). The majority of these layers or blocks are in sharp contact with gneisses and schists by faulting (Figure 2e). Some amphibolites (e.g., 19S72-1, 19S73-1, 19S73-2, and 19S74-1) are accompanied by serpentinite and are in fault contact with the Bt-Ms schist (Figure 2d). A felsic rock sample (19S64-2) collected from the Batang area intruded into massive amphibolite (19S64-1; Figure 2c). Detailed sample localities are shown in Figure 1b. The abbreviations of the mineral are the same as those of Whitney and Evans [79].

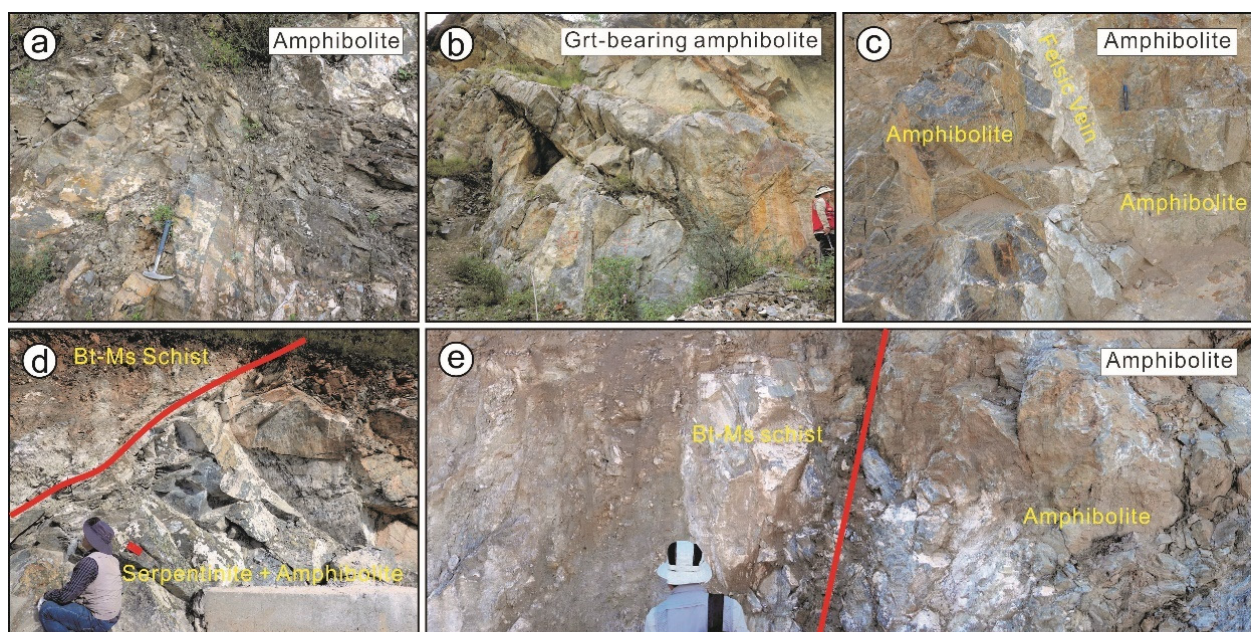
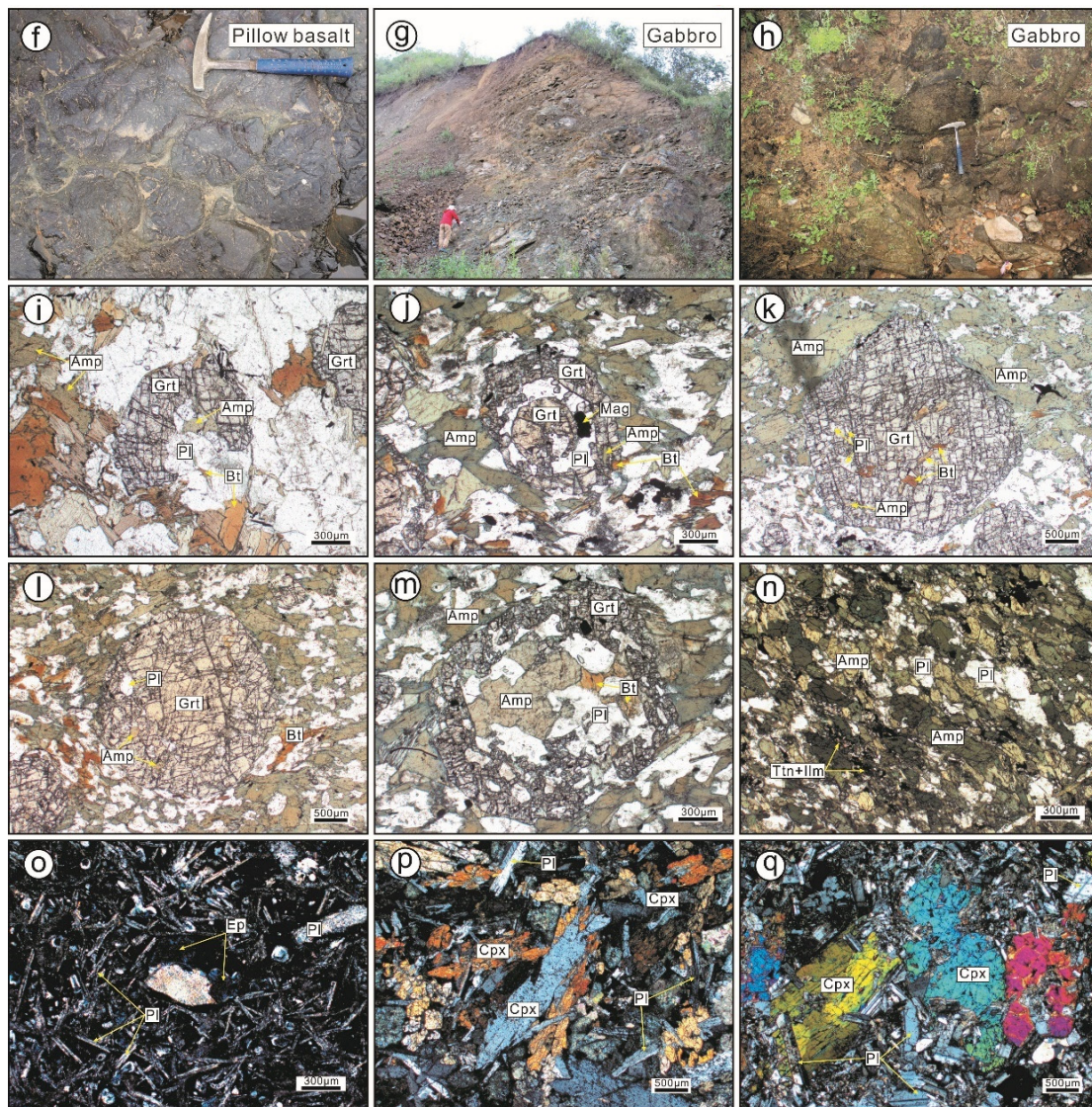


Figure 2. Cont.



**Figure 2.** (a–h) Field photographs and (i–q) photomicrographs of mafic and metamafic rocks in the JASB. (a) Amphibolite in the Batang area; (b) Bedded Grt-bearing amphibolite in the Batang area; (c) Amphibolite intruded by felsic vein in the Batang area; (d) Amphibolite is accompanied by serpentinite and in contact with Bt-Ms schist by the fault in the Batang area; (e) Amphibolite is in sharp contact with Bt-Ms schist by the fault in the Batang area; (f) Pillow basalt in the Yaxuanqiao area; (g) Massive gabbro in the Yaxuanqiao area; (h) Gabbro in the Lvchun area; (i) Garnet in Grt-Bt amphibolite alternating with amphibole, plagioclase, and biotite; (j) Multiple atoll microstructures of garnet in Grt-Bt amphibolite with BSE image; (k,l) Euhedral and subhedral garnet in Grt-Bt amphibolite with inclusions of plagioclase, biotite, and amphibole in core and rim, respectively; (m) Euhedral atoll garnet in Grt-Bt amphibolite; (n) Dark green amphibolite with oriented amphibole and plagioclase; (o) Basalt with altered clinopyroxene phenocryst in the Yaxuanqiao area; (p) Fresh gabbro in the Yaxuanqiao area; (q) Porphyritic gabbro in the Lvchun area.

The basalt shows a porphyritic texture (Figure 2o). Most phenocrysts are coarse chlorogenic clinopyroxenes, and the matrix is mainly plagioclase and fine chlorogenic clinopyroxenes. The gabbro from the Yaxuanqiao area is largely composed of euhedral to subhedral coarse clinopyroxene (40%–45%) and plagioclase (50%–55%). Clinopyroxene is partly altered to chlorite along fractures and plagioclase to microcrystalline epidote (Figure 2p). The gabbro from the Lvchun area shows porphyroid texture, and it consists of clinopyroxene phenocrysts (50%–60%), fine plagioclase matrix (35%–40%), and minor magnetite (<5%) (Figure 2q).

The (Grt-) amphibolites generally contain Grt (0%–5%), Amp (45%–80%), Pl (20%–45%), and Bt (5%–10%; Figure 2i–n). Some metamorphic garnets display microstructures such as corona texture, atoll structure, and embayment texture (Figure 2i,j,m). The porphyroblastic garnet crystal (1–3 mm) rims preserve abundant inclusions, such as biotite, plagioclase, amphibole, ilmenite, apatite, and rutile (Figure 2k). Garnet from Grt-amphibolite (19S60-7) consists predominantly of almandine ( $X_{\text{Alm}} = 0.61\text{--}0.66$ ), grossular ( $X_{\text{Grs}} = 0.15\text{--}0.21$ ), and pyrope ( $X_{\text{Prp}} = 0.13\text{--}0.18$ ), with minor spessartine ( $X_{\text{Sps}} = 0.03\text{--}0.04$ ). Garnet grains show near-constant contents from core to rim (Figure 3a). Brown amphibole in the matrix from Grt-amphibolite is tschermakite and sadanagaite ( $^{\text{B}}\text{Ca} = 1.81\text{--}1.91$ ;  $^{\text{A}}[\text{Na}+\text{K}] = 0.40\text{--}0.51$ ;  $\text{Si} = 6.22\text{--}6.32$  p.f.u.;  $X_{\text{Mg}} = 0.47\text{--}0.54$ ; Figure 3b; [80]). In most cases, amphiboles occurring as inclusion in garnet have composition similar to those of matrix amphibole. The end-members of plagioclase were normalized based on  $X_{\text{An}}$ ,  $X_{\text{Ab}}$ , and  $X_{\text{Or}}$ . Matrix plagioclase has  $X_{\text{An}}$  of 0.37–0.83,  $X_{\text{Ab}}$  of 0.17–0.62 and  $X_{\text{Or}}$  of 0.00–0.03 (Figure 3c). Plagioclase grains exhibit compositional zoning with an increase in  $X_{\text{Ab}}$  and a decrease  $X_{\text{An}}$  from core to rim. Plagioclase inclusions in garnet show similar composition to those of matrix plagioclase. Biotites are dominated by ferribiotite and magnesian biotite, with  $\text{FeO}^{\text{T}}$  and  $\text{MgO}$  contents ranging from 21.63–30.97 wt.% and 7.34–10.58 wt.%, respectively. The  $\text{TiO}_2$  contents vary from 0.09–3.30 wt.%. The  $\text{MgO}$  contents exhibit an opposite trend to  $\text{FeO}^{\text{T}}$  (Figure 3d).

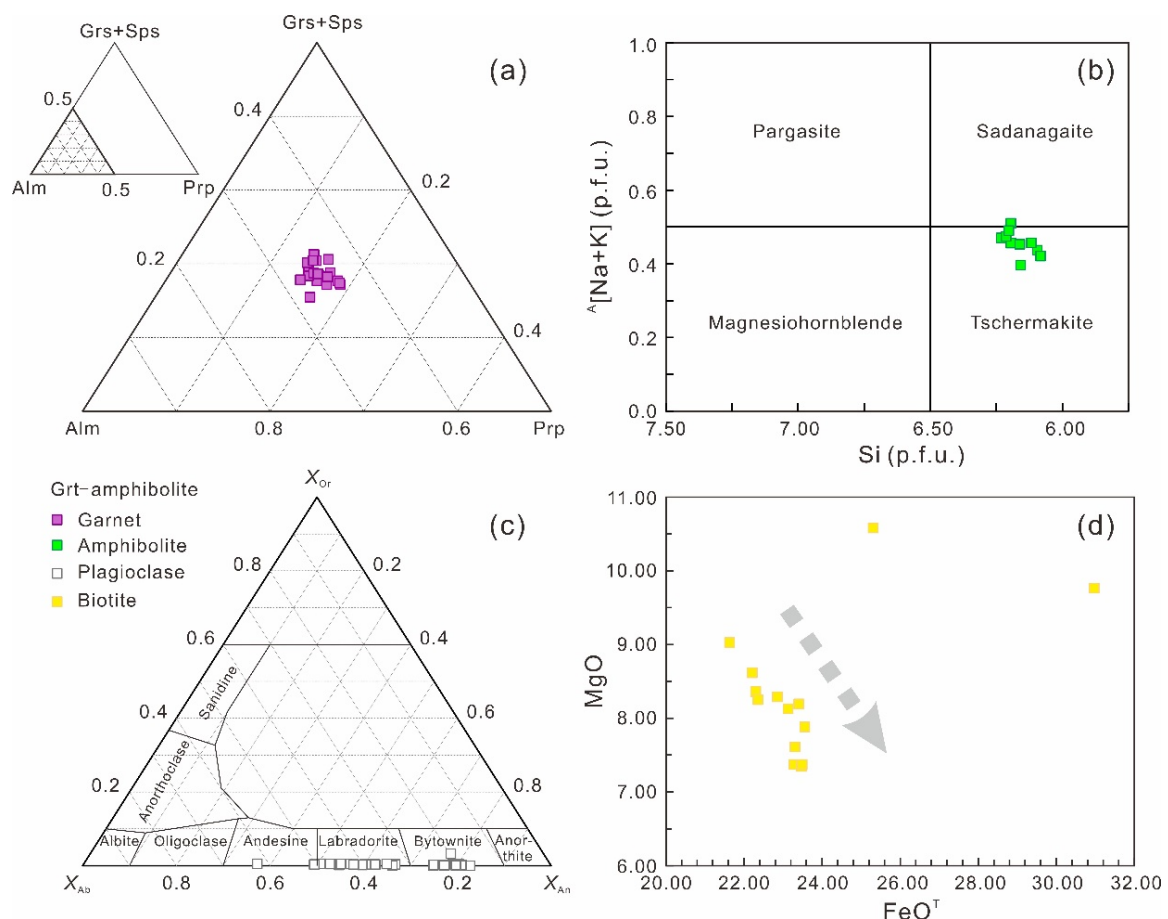


**Figure 3.** Compositional variation of Principal minerals from Grt-amphibolite from the JASB. (a) Alm vs. Prp vs. Grs + Sps ternary diagrams of garnet from Grt-amphibolite. (b) Si vs.  $^{\text{A}}[\text{Na}+\text{K}]$  classification diagram for amphibole [80]. (c)  $X_{\text{Ab}}$  vs.  $X_{\text{An}}$  vs.  $X_{\text{Or}}$  classification diagram for plagioclase. (d)  $\text{FeO}^{\text{T}}$  vs.  $\text{MgO}$  diagram for biotite.

On the basis of the mineral paragenesis of the Grt-amphibolite, conventional garnet-hornblende-plagioclase-quartz (GHPQ) geothermobarometers (with an uncertainty of  $\pm 45$  °C/ $\pm 1$  kbar; [81,82]), Ti-in-biotite thermometer (with an uncertainty of  $\pm 25$  °C; [83]) and Al-in-amphibolite barometer (with an uncertainty of  $\pm 2$  kbar; [84]) were employed to evaluate their peak metamorphic conditions. To determine meaningful peak *P-T* conditions (M2), rim compositions were selected for homogeneous garnet. For amphibole and plagioclase, core compositions were used to minimize the effect of diffusion during cooling and retrograde metamorphism. As a result, temperatures and pressures obtained from the Grt-amphibolite (19S60-7) are 591–730 °C/5.1–7.0 kbar (Supplementary Table S1).

#### 4. Materials and Methods

##### 4.1. SHRIMP Zircon U–Pb Dating

The U–Pb analyses of 19S61-3, 19S64-1, and 18J33-1 were performed using a sensitive high-resolution ion microprobe (SHRIMP) II at the Beijing SHRIMP Center, Institute of Geology, CAGS, China. After these fresh samples were crushed, the zircon was separated using heavy liquid and magnetic separation methods. Then, the zircons were extracted from each crushed-rock sample by hand-picking under a binocular microscope. The zircon grains were mounted in epoxy resin discs and then sectioned and polished to reveal their cross-sections. Zircons from each sample were mounted separately with a fragment of the standard zircon PLE (337 Ma; [85]). The analytical procedures were similar to those described by Williams [86]. The SHRIMP runs used a primary ion beam of ca. 4.5–6.5 nA, with 10 kV of O<sup>2-</sup> focused to a ca. 25- $\mu$ m-diameter spot. Each spot was rastered for 120–180 s prior to analyses. Common Pb corrections were based on the measured <sup>204</sup>Pb/<sup>206</sup>Pb ratios, as described in Compston et al. [87]. Weighted mean ages of individual samples are quoted at the 95% confidence level, whereas the uncertainties for individual analyses are quoted at the 1 $\sigma$  level.

##### 4.2. LA–ICP–MS Zircon U–Pb Dating

Several samples (19S61-4, 19S64-1, 19S64-2, and 19S71-1) from the Batang area were selected for LA–ICP–MS zircon U–Pb dating. U–Pb analyses of magmatic zircons from the samples were conducted by laser ablation LA–ICP–MS at Beijing Geoanalyses Co., Ltd. (Beijing, China). An Agilent 7900 ICP–MS instrument (Agilent, Santa Clara, CA, USA) with a Resolution SE model laser ablation system (Applied Spectra, Fremont, CA, USA) was used to acquire ion-signal intensities. The laser beam diameter was 24  $\mu$ m and operated at a frequency of 5 Hz. Each analysis consisted of approximately 20 s of background acquisition and 35–40 s of data acquisition. The calibration of Pb/U ratios is relative to the standard zircon Plešovice [85], which was analyzed once every 10–15 samples. The Lolite software package was used for the data processing [88]. Concordia diagrams, weighted average age calculations, and probability density plotting were conducted using Isoplot 4.15 [89].

##### 4.3. Zircon Lu–Hf Isotopes

The zircon in situ Hf isotope compositions were determined by LA–MC–ICP–MS at the Nanjing Hongchuang Exploration Technology Service Co., Ltd. (Nanjing, China). Hf isotope measurements were performed on the same spot or the same age domains for zircon grains with concordant U–Pb ages. A stationary spot was used for analyses with a beam diameter of 45  $\mu$ m, repetition rate of 6 Hz, energy density of ca. 4 J/cm<sup>2</sup>, and an ablation time of 30 s. The measured <sup>176</sup>Hf/<sup>177</sup>Hf ratios were normalized to <sup>176</sup>Hf/<sup>177</sup>Hf = 0.7325, using exponential correction for mass bias. Isobaric interference of <sup>176</sup>Yb and <sup>176</sup>Lu on <sup>176</sup>Hf was corrected by monitoring <sup>173</sup>Yb and <sup>175</sup>Lu, respectively. The in situ measured <sup>173</sup>Yb/<sup>171</sup>Yb ratio was used for the mass bias correction for both Yb and Lu. The ratios used for the corrections are 0.7963 for <sup>176</sup>Yb/<sup>173</sup>Yb and 0.02655 for <sup>176</sup>Lu/<sup>175</sup>Lu [90].  $\epsilon$ Hf(t) values were calculated with chondritic values of

$^{176}\text{Hf}/^{177}\text{Hf} = 0.282772$  and  $^{176}\text{Lu}/^{177}\text{Hf} = 0.0332$  [91] at the zircon ages. The single-stage Hf model ages ( $T_{\text{DM1}}$ ) and two-stage model ages ( $T_{\text{DM2}}$ ) were calculated relative to the depleted mantle with present-day  $^{176}\text{Hf}/^{177}\text{Hf} = 0.28325$  and  $^{176}\text{Lu}/^{177}\text{Hf} = 0.0384$  [92] and an average continental crust  $^{176}\text{Lu}/^{177}\text{Hf}$  value (0.015).

#### 4.4. Whole-Rock Geochemistry and Sm–Nd Isotopes

The fresh samples were crushed to 200-mesh in a steel mortar and ground in a steel mill for the elemental and isotopic analyses. The major element analyses were performed by using a PW4400-type XRF spectrometer based on the Chinese national standard GB/T 14506.30-2010 at the ALS Chemex Company in Guangzhou, China. The analytical uncertainties of the XRF analyses were estimated to be  $\pm 3\%$ – $5\%$  for major oxides with concentrations  $>0.5\%$ . Trace element abundances were measured by the Agilent 7500a ICP–MS instrument platform. The detailed sample-digesting procedures for the ICP–MS analyses and the analytical precision and accuracy for trace elements are the same as those in Liu et al. [93]. Most of the illustrations in this paper were produced using GEOKIT software [94].

The Sm and Nd isotopic compositions were determined by using a Finnigan MAT-262 multicollector mass spectrometer (Bremen, Germany) instrument at the Laboratory for Radiogenic Isotope Geochemistry, University of Science and Technology of China (USTC). Procedural blanks were  $<50$  pg for Sm and Nd.  $^{143}\text{Nd}/^{144}\text{Nd}$  values were corrected for mass fractionation by normalization to  $^{146}\text{Nd}/^{144}\text{Nd} = 0.7219$ . The precision of the  $^{147}\text{Sm}/^{144}\text{Nd}$  ratios was better than  $0.5\%$ , and the accuracy of the measured Nd isotopic ratios was better than  $0.003\%$ . Details of the experimental procedures and the analytical precision were discussed by Liang et al. [95].

## 5. Results

### 5.1. SHRIMP Zircon U–Pb Ages

Zircons from sample 19S61-3 are euhedral, translucent, and prismatic. Most zircon grains are 200 to 300  $\mu\text{m}$  and have a narrow metamorphic rim (Figure 4a). The zircon cores show weak oscillatory growth zoning and dark-gray homogenous patterns in cathodoluminescence (CL) images with Th/U ratios ranging from 0.13 to 0.67, suggesting a magmatic origin. We performed 30 analyses by SHRIMP. A total of 28 analyses yield a weighted mean  $^{206}\text{Pb}/^{238}\text{U}$  age of  $231.7 \pm 2.4$  Ma ( $1\sigma$ , MSWD = 1.4, Figure 4a), which is interpreted as the crystallization age of these rocks. The remaining two analyses (spots 25 and 28) may suffer Pb loss or inclusion.

For the U–Pb analyses, the thirty zircon grains from sample 19S64-1 are mostly euhedral, transparent to colorless, and stubby to elongate in shape, with lengths of 100 to 250  $\mu\text{m}$  and widths of 50 to 150  $\mu\text{m}$  (Figure 4b). Most grains have a core-rim texture, while the CL images show light-gray patterns and patch texture in the rim and dark-gray patterns and oscillatory zoning in the core. Twenty analyses in the core give a weighted mean  $^{206}\text{Pb}/^{238}\text{U}$  age of  $265.8 \pm 1.9$  Ma ( $1\sigma$ , MSWD = 1.4, Figure 4b), and Th/U ratios range from 0.15 to 0.32 except for 16 and 27 spots. We interpret this age as the crystallization age of this rock. The zircon rim has low U and high common Pb contents. Ten analyses of the rim yield  $^{206}\text{Pb}/^{238}\text{U}$  ages between 236.9 Ma and 273 Ma, with high error values (ranging from 4.2 to 11, Supplementary Table S5), which are meaningless for the rock.

Thirty zircon grains from gabbro sample 18J33-1 are euhedral, transparent, and prismatic or tabular, with lengths of 100 to 150  $\mu\text{m}$  and widths of 50 to 80  $\mu\text{m}$ . All zircon grains show a gray pattern without oscillatory zoning according to CL images (Figure 4c). Thirty analyses give a weighted mean  $^{206}\text{Pb}/^{238}\text{U}$  age of  $236.9 \pm 3.0$  Ma ( $1\sigma$ , MSWD = 6.5, Figure 4c), and Th/U ratios range from 1.63 to 4.93. Therefore, this age is interpreted as the crystallization age of the gabbro.

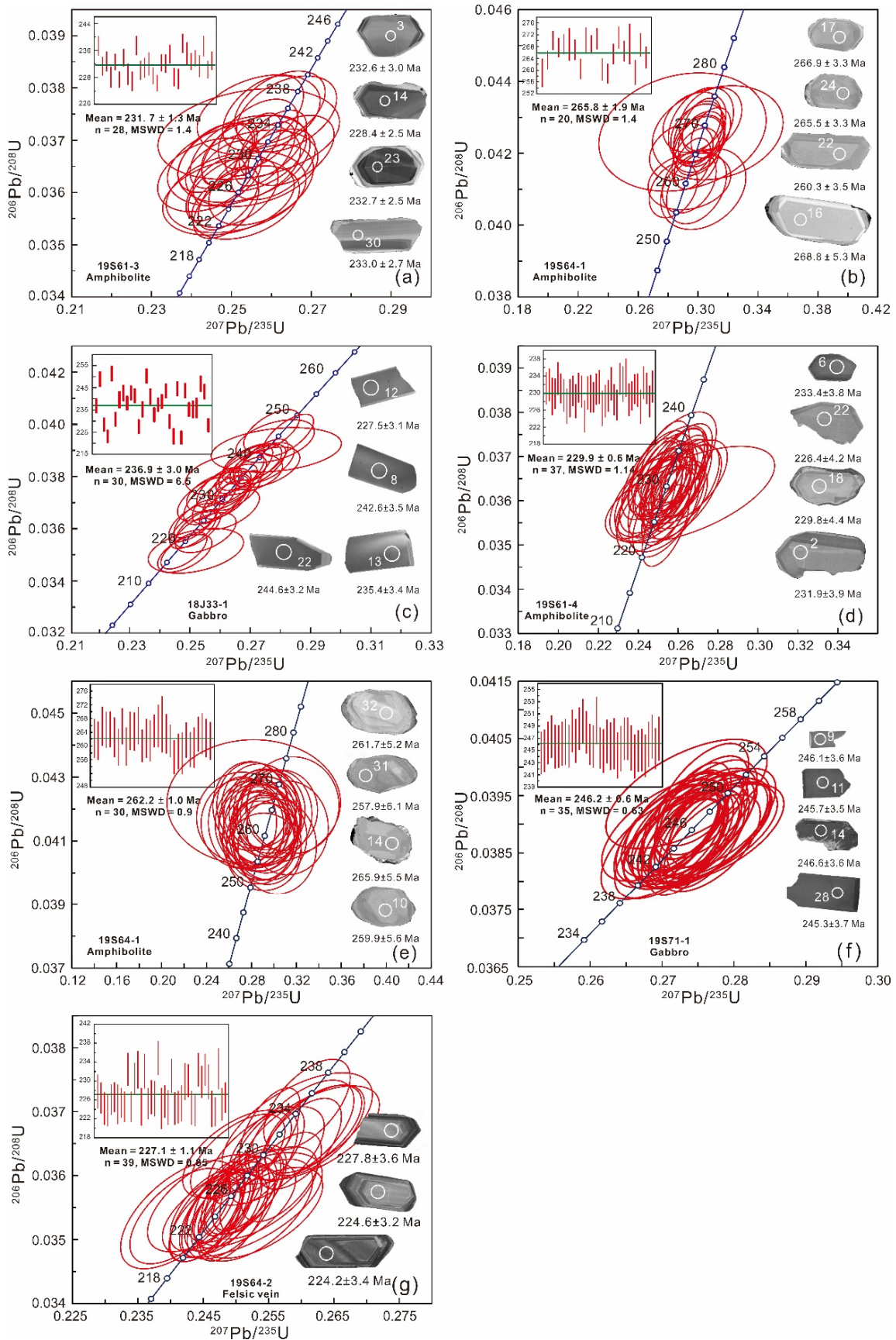


**Figure 4.** (a–c) Sensitive High-Resolution Ion Microprobe (SHRIMP) and (d–g) laser ablation inductively coupled plasma mass spectrometry (LA-ICP-MS) zircon U–Pb concordia diagrams with representative zircon images for the amphibolites from the JASB.

### 5.2. LA-ICP-MS Zircon U-Pb Ages

Sample 19S61-4 was collected for LA-ICP-MS zircon U-Pb dating (Supplementary Table S6 and Figure 4d). Zircon grains are mainly subhedral, transparent to colorless, and columnar or tabular, with grain sizes of 100 to 250  $\mu\text{m}$ . All the zircons have broadly spaced oscillatory zoning and moderate Th/U ratios (0.26–0.51). Thirty-seven analyses yielded a weighted mean  $^{206}\text{Pb}/^{238}\text{U}$  age of  $229.9 \pm 0.6$  Ma (1 $\sigma$ , MSWD = 1.14, Figure 4d), which is interpreted as the crystallization age of this rock.

Forty zircon grains from sample 19S64-1 were also analyzed by LA-ICP-MS. Thirty analyses yielded a weighted mean  $^{206}\text{Pb}/^{238}\text{U}$  age of  $262.2 \pm 1.0$  Ma (1 $\sigma$ , MSWD = 0.9, Figure 4e), with moderate Th/U ratios (0.15 to 0.70). This age is interpreted as the crystallization age of this rock.

Sample 19S64-2 was collected from felsic veins that intruded into the rock of sample 19S64-1 (Figure 2c). All zircons are euhedral, transparent, columnar, or tabular, with grain sizes of 100 to 300  $\mu\text{m}$ . The zircons show weak oscillatory growth zoning and dark-gray homogenous patterns in CL images with Th/U ratios ranging from 0.25 to 0.56 (Figure 4g). We performed a total of 40 analyses. Thirty-nine analyses yielded a weighted mean  $^{206}\text{Pb}/^{238}\text{U}$  age of  $227.1 \pm 1.1$  Ma (1 $\sigma$ , MSWD = 0.85, Figure 3g), which is interpreted as the crystallization age of the felsic rock.

Zircons from gabbro sample 19S71-1 are mainly euhedral to subhedral, transparent, columnar or tabular, with grain sizes of 80 to 200  $\mu\text{m}$ . Most zircons have broadly spaced oscillatory zoning and high Th/U ratios (0.82–1.76), except for num. 31 spot. Thirty-five analyses yielded a weighted mean  $^{206}\text{Pb}/^{238}\text{U}$  age of  $246.2 \pm 0.6$  Ma (1 $\sigma$ , MSWD = 0.63, Figure 4f). This age represents the crystallization age of the gabbro.

### 5.3. Zircon in Situ Hf Isotopes

Zircon grains from six samples (e.g., 19S61-3, 19S61-4, 19S64-1, 19S64-2, 19S71-1, and 18J33-1) were analyzed for Lu-Hf isotopes on the same domains or zircons with structures similar to those analyzed for U-Pb dating.  $\epsilon\text{Hf}(t)$  values,  $T_{\text{DM1}}$ , and  $T_{\text{DM2}}$  were calculated for their zircon U-Pb ages. The results are listed in Supplementary Table S4.

For the zircons from samples 19S61-3 and 19S61-4 of the Batang amphibolite, we performed 34 and 44 analyses, respectively. Their analytical results show similar Hf isotope compositions, with  $\epsilon\text{Hf}(t)$  values ranging from  $-7.90$  to  $+1.01$  and most  $\epsilon\text{Hf}(t)$  values are less than  $-3.00$ , corresponding to single-stage Hf model ages ( $T_{\text{DM1}}$ ) of 1208–838 Ma.

Thirty-eight zircons from sample 19S64-1 of the Batang amphibolite yield narrowly positive  $\epsilon\text{Hf}(t)$  values of  $+14.54$  to  $+16.80$ . Their single-stage Hf model ages ( $T_{\text{DM1}}$ ) range from 316 to 231 Ma.

Forty-five zircons from sample 19S64-2 of the felsic vein show negative  $\epsilon\text{Hf}(t)$  values ranging from  $-8.73$  to  $-5.32$ , except one zircon with an  $\epsilon\text{Hf}(t)$  value of  $-28.70$ . Their single- and two-stage Hf model ages ( $T_{\text{DM1}}$  and  $T_{\text{DM2}}$ ) range from 1231–1111 Ma and 1814–1594 Ma, respectively.

Forty-two zircons from sample 19S71-1 of the Batang gabbro show variable  $\epsilon\text{Hf}(t)$  values ranging from  $-4.27$  to  $+8.53$ , corresponding to single-stage Hf model ages ( $T_{\text{DM1}}$ ) of 1102–645 Ma.

Thirty zircons from sample 18J33-1 of the Lvchun gabbro have broadly positive  $\epsilon\text{Hf}(t)$  values ranging from  $+4.64$  to  $+14.15$ . Their single-stage Hf model ages ( $T_{\text{DM1}}$ ) range from 691 to 325 Ma.

### 5.4. Whole-Rock Geochemical and Sm-Nd Isotope Compositions

Samples from the Jinshajiang and Ailaoshan orogenic belts are classified into five groups and two groups, respectively, by their petrographic and geochemical signatures, and ages. Major oxide and trace element data for the samples are listed in Supplementary Table S2. The Sm-Nd isotopic ratios are recalculated to their crystallization ages determined by zircon U-Pb geochronology and ages determined in previous studies. The analytical results of Sm-Nd isotopes are listed in Supplementary Table S3.

#### 5.4.1. Jinshajiang Metamafic Rocks

Group 1 (19S64-1, 19S73-2) displays a narrow compositional range ( $\text{SiO}_2 = 48.00\text{--}49.55$  wt.%,  $\text{Al}_2\text{O}_3 = 15.56\text{--}16.11$  wt.%,  $\text{FeO}^T = 7.48\text{--}9.18$  wt.%,  $\text{MgO} = 6.93\text{--}7.78$  wt.%,  $\text{CaO} = 11.25\text{--}11.95$  wt.%,  $\text{Na}_2\text{O} = 2.27\text{--}2.79$  wt.%,  $\text{TiO}_2 = 0.97\text{--}1.29$  wt.%), and both samples belong to the calc-alkaline series (Figure 5b). They have LREE-enriched patterns ( $(\text{La}/\text{Yb})_N = 2.31\text{--}3.91$ ), negligible negative Eu anomalies ( $\text{Eu}/\text{Eu}^* = 0.83$  to  $0.89$ ), and plot like E-MORB in chondrite-normalized rare earth element (REE) pattern (Figure 6c) with slightly enriched large ion lithophile elements (LILE) and nonsignificant Nb and Ta anomalies (Figure 6d). One sample from this group (19S64-1) gives a positive  $\epsilon\text{Nd}(t)$  value (+6.95, Supplementary Table S3).

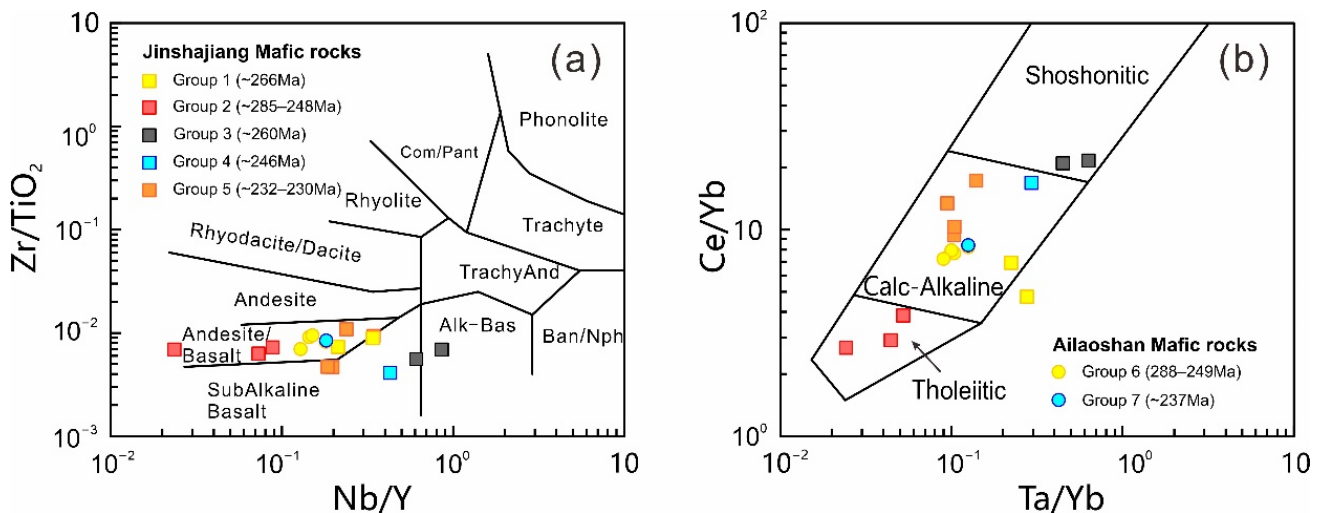


**Figure 5.** (a) Nb/Y vs. Zr/TiO<sub>2</sub> diagram [96] and (b) Ta/Yb vs. Ce/Yb diagram [97] for mafic and metamafic rocks from the JASB.

Group 2 (19S72-1, 19S73-1, 19S74-1) has relatively high  $\text{SiO}_2$  (48.52–50.33 wt.%) but low  $\text{Al}_2\text{O}_3$  (14.10–16.10 wt.%),  $\text{FeO}^T$  (7.85–12.05 wt.%),  $\text{MgO}$  (7.24–7.92 wt.%),  $\text{CaO}$  (7.27–10.35 wt.%),  $\text{Na}_2\text{O}$  (2.92–3.11 wt.%),  $\text{K}_2\text{O}$  (0.22–0.74 wt.%), and  $\text{TiO}_2$  (1.16–1.97 wt.%) contents. The  $\text{Mg}^\#$  values ( $100 \times \text{MgO}/(\text{MgO} + \text{FeO}^T)$ ) range from 54–62. Nb/Y vs. Zr/TiO<sub>2</sub> and Ta/Yb vs. Ce/Yb diagrams show that they are similar to tholeiitic basalts (Figure 5a,b). These samples show N-MORB-like REE normalized patterns, but are enriched in LILE (e.g., Rb, Ba, U, K), and depleted in HFSE (e.g., Th, Nb, Ta, Zr, Hf) with slightly negative Eu anomalies (Figure 6c,d). These rocks have relatively more depleted  $\epsilon\text{Nd}(t)$  values (+6.57 to +8.88, Supplementary Table S3) with an assumed age of 265 Ma.

Group 3 (19S60-2, 19S61-2) exhibits relatively low  $\text{SiO}_2$  (46.45–48.87 wt.%),  $\text{Al}_2\text{O}_3$  (13.69–15.90 wt.%),  $\text{MgO}$  (4.45–4.53 wt.%),  $\text{CaO}$  (8.58–8.59 wt.%), high  $\text{TiO}_2$  (2.82–3.21 wt.%),  $\text{FeO}^T$  (13.16–14.38 wt.%), and  $\text{K}_2\text{O}$  (1.37–1.38 wt.%); and variable  $\text{Na}_2\text{O}$  (0.72–2.76 wt.%) and  $\text{P}_2\text{O}_5$  (0.59–1.01 wt.%). These samples define typical alkaline basalts on the Nb/Y vs. Zr/TiO<sub>2</sub> diagram (Figure 5a) and shoshonitic compositional trends on the Ta/Yb vs. Ce/Yb diagram (Figure 5b). These mafic rocks show chondrite-normalized REE and primitive mantle-normalized trace element patterns similar to those of ocean island basalt (OIB; Figure 6a,b), and strongly enriched LREE contents and minor Eu anomalies ( $\text{Eu}/\text{Eu}^* = 0.99\text{--}1.21$ ). These rocks have slightly negative  $\epsilon\text{Nd}(t)$  values of  $-0.54$  to  $-0.70$  (Supplementary Table S4).

Group 4 (19S71-1) exhibits relatively low  $\text{SiO}_2$  (48.26%),  $\text{Al}_2\text{O}_3$  (13.14%),  $\text{MgO}$  (3.58%), and  $\text{CaO}$  (7.77%) contents and  $\text{Mg}^\#$  (31) value and high  $\text{TiO}_2$  (3.00%) and  $\text{FeO}^T$  (14.29%) contents. Nb/Y vs. Zr/TiO<sub>2</sub> and Ta/Yb vs. Ce/Yb diagrams define a typical calc-alkaline composition (Figure 5a,b). This sample has enriched LREE and LILE (Rb, Th, and U) and depleted HFSE (e.g., Nb, Ta, Zr, and Hf) with nonsignificant negligible Eu anomalies ( $\text{Eu}/\text{Eu}^* = 0.86$ ; Figure 6c,d).

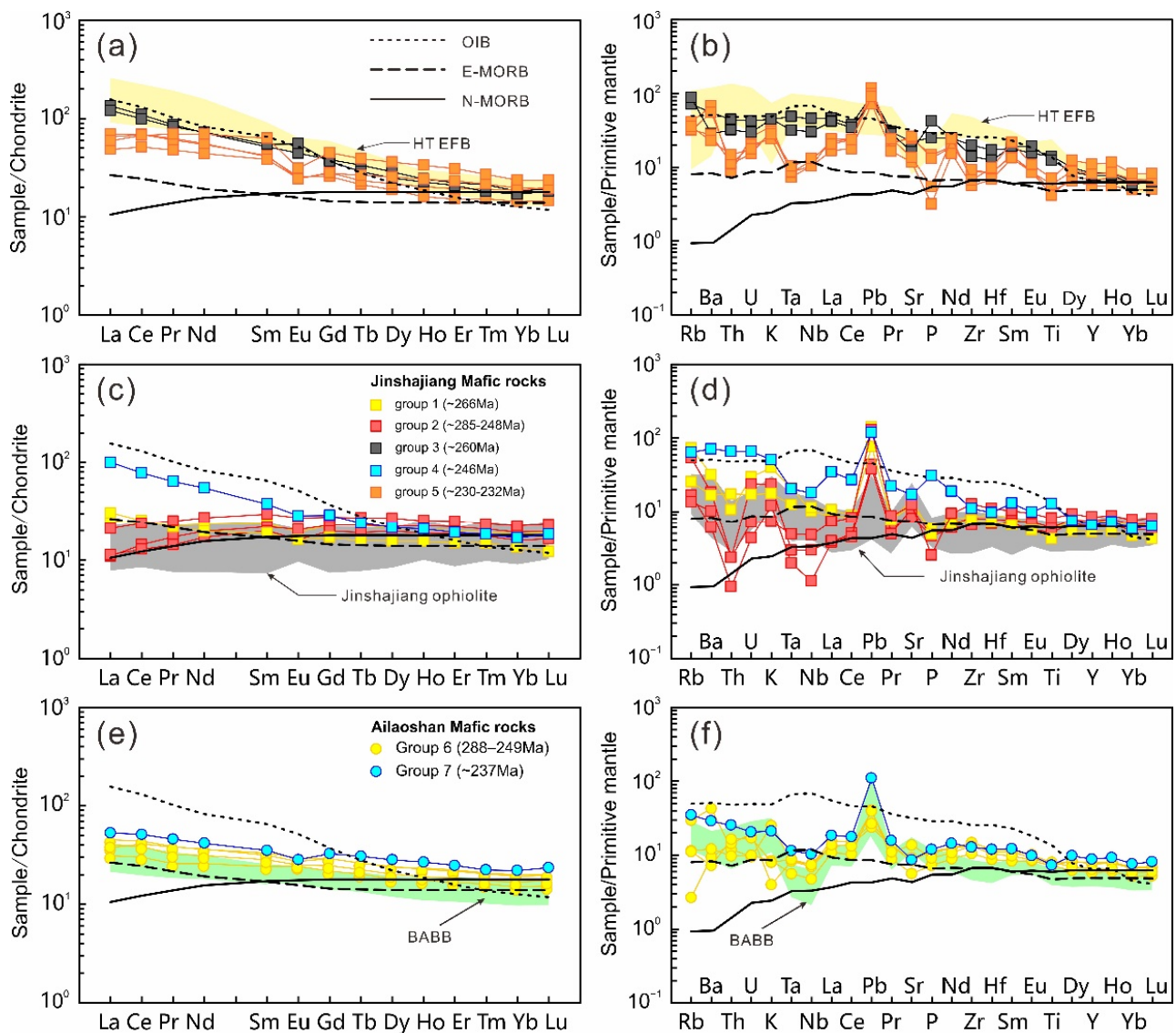


**Figure 6.** (a,c,e) Chondrite-normalized REE patterns and (b,d,f) primitive mantle-normalized trace element patterns for mafic and metamafic rocks from the JASB. Normalized values for primitive mantle and chondrite are from [98]. Data for N-MORB, E-MORB, and OIB are from [98].

Group 5 (19S60-5, 19S60-7, 19S61-3, 19S61-4) displays small variations in major oxide compositions with  $\text{SiO}_2 = 44.42\text{--}46.51$  wt.%,  $\text{FeO}^{\text{T}} = 11.36\text{--}12.87$  wt.%,  $\text{Na}_2\text{O} = 1.30\text{--}2.24$  wt.%,  $\text{K}_2\text{O} = 0.80\text{--}1.09$  wt.%, and  $\text{TiO}_2 = 0.94\text{--}1.60$  wt.%, except for variable  $\text{MgO}$  (4.71–8.35 wt.%) and  $\text{Al}_2\text{O}_3$  (15.20–21.00 wt.%). This group defines a calc-alkaline basalt compositional trend on the Nb/Y vs. Zr/TiO<sub>2</sub> and Ta/Yb vs. Ce/Yb diagrams (Figure 5a,b). The  $\text{Mg}^{\#}$  values range from 39–57. The 19S60-5 and 19S60-7 samples have extremely lower Cr (1–10 ppm) and Ni (1.0–4.6 ppm) contents and higher  $\text{Al}_2\text{O}_3$  than the other two samples. These rocks show LREE and LILE enrichment and pronounced Nb, Ta, Zr, and Hf depletion relative to La, Nd, and Sm (Figure 6a,b), with significant Eu anomalies ( $\text{Eu}/\text{Eu}^* = 0.58\text{--}0.77$ ). Meanwhile, they have negative  $\epsilon\text{Nd}(t)$  values (−5.14 to −6.77), which are much lower than those of the Group 1 in this study (Supplementary Table S3).

#### 5.4.2. Ailaoshan Mafic Rocks

Group 6 (17HA21-1, 18J18-1, 18J24-1, and 18J28-1) collected from the Yaxuanqiao volcanic arc contains relatively low  $\text{SiO}_2$  (45.64–49.95 wt.%) and  $\text{TiO}_2$  (1.65–1.82 wt.%), and variable  $\text{Al}_2\text{O}_3$  (11.76–16.14 wt.%),  $\text{MgO}$  (5.34–14.65 wt.%), and  $\text{Na}_2\text{O}$  (1.29–4.56 wt.%) con-

tents. Group 6 exhibits a calc-alkaline series on the Nb/Y vs. Zr/TiO<sub>2</sub> and Ta/Tb vs. Ce/Yb diagrams (Figure 5a,b). This group of rocks shows LREE and LILE enrichment and Nb, Ta, Zr, and Hf depletion on the chondrite-normalized REE and primitive mantle-normalized trace element patterns, which are similar to those of E-MORB (Figure 6e,f). These E-MORB-like rocks have positive  $\epsilon\text{Nd}(t)$  values of +5.07 to +4.99 with a reference age of 288 Ma from Fan et al. [48].

Group 7 (18J33-1) collected from the Lvchun area contains relatively high SiO<sub>2</sub> (50.03 wt.%), Al<sub>2</sub>O<sub>3</sub> (16.50 wt.%), and CaO (10.50 wt.%) contents and low TiO<sub>2</sub> (1.70 wt.%), MgO (5.01 wt.%), Na<sub>2</sub>O (2.60 wt.%), and K<sub>2</sub>O (0.64 wt.%) contents. Nb/Y vs. Zr/TiO<sub>2</sub> and Ta/Yb vs. Ce/Yb diagrams show that this group is similar to the calc-alkaline series (Figure 5a,b). This rock displays LREE- and LILE-enriched chondrite-normalized REE and primitive mantle-normalized trace element patterns and slightly negative Nb and Ta anomalies (Figure 6e,f). The rock has a slightly negative  $\epsilon\text{Nd}(t)$  value of −1.51 (Supplementary Table S3) and positive zircon in situ  $\epsilon\text{Hf}(t)$  values of +4.64 to +14.15 (Supplementary Table S4).

## 6. Discussion

### 6.1. Geochronology Outline of Major Tectonothermal Events

Although abundant mafic-felsic and metamorphic rocks have been reported along the JASB (Supplementary Tables S7 and S8), and Wang et al. [9] reviewed the tectonic evolution of eastern Cimmerian and Southeast Asia, the spatial and temporal distributions of these magmatic and metamorphic events are still debated. In this study, containing our and reference data, we collated 232 reliable weighted mean U–Pb and Sm–Nd crystallization ages of mafic-felsic rocks, and 51 weighted-mean U–Pb and Ar–Ar metamorphic ages from the Jinshajiang, Ailaoshan, and Song Ma areas to reconstruct the Early Permian to Late Triassic geochronological history of the JASB (Figure 7). In summary, their geochronological signature suggests that three periods of Paleo-Tethyan magmatism and one period of metamorphism occurred in the JASB, as described below.

#### 6.1.1. ~288–248 Ma Arc/Back-Arc Basin Magmatism

The products of Early Permian–Early Triassic magmatism are clearly widespread in the JASB. Most of these rocks were exposed in the areas of the Jomda–Weixi volcanic belt to the north and the Yaxuanqiao–Truong Son volcanic belt and DAMB to the south (Figure 1b). They are composed of mafic intrusions (e.g., gabbro and diabase), granitoids (e.g., granodiorite, tonalite, diorite, monzogranite, and gneissic granite), and volcanic rocks (e.g., basalt, andesite, dacite, and rhyolite; Supplementary Table S7). In this study, we collated 73 published U–Pb age samples from previous studies and this study, which yield weighted mean ages of ca. 285–248 Ma, ca. 288–249 Ma, and ca. 277–265 Ma from the Jinshajiang, Ailaoshan, and Song Ma orogenic belts, respectively (Figure 7). In summary, this stage of mafic and felsic magmatism along the JASB formed simultaneously, which argues for the development of a Permian to Early Triassic arc/back-arc basin setting (e.g., [5,19,48,50]). However, some studies consider that the ca. 260–250 Ma magmatism may represent an arc-continent collisional setting, as suggested by the regional sedimentary unconformity, and I- and S-type granitoids in the western Ailaoshan volcanic belt and Truong Son belt (e.g., [24]). Therefore, this period of magmatism needs to be discussed in detail based on geochronological and geochemical data.

#### 6.1.2. ~248–237 Ma Orogenic Magmatism

The rocks from this period of magmatism are mainly distributed in the Jomda–Weixi volcanic belt, Ailaoshan metamorphic complex belt, and Truong Son volcanic belt, with a few samples in the Batang, Xumai, Lvchun, and Yaxuanqiao areas (Figure 1b). In this study, we collate 32 reliable weighted mean U–Pb ages, in which there are clearly more felsic rock samples than mafic rock samples (Figure 7). These mafic and felsic rocks give strong peak ages of ca. 245–240 Ma (Figure 7), suggesting that a notable magmatic process and tectonic evolution stage occurred during this period. Yang et al. [43] reported

Late Paleozoic to Early Mesozoic magmatic activity along the Jomda–Weixi–Yunxian areas, which have a continental arc-like affinity. However, some other studies suggested that the products of magmatism during this period probably occurred in a syncollisional setting (e.g., [24,99,100]). Therefore, such a relationship with Middle Triassic magmatism in the JASB and their tectonic setting need to be carefully considered.

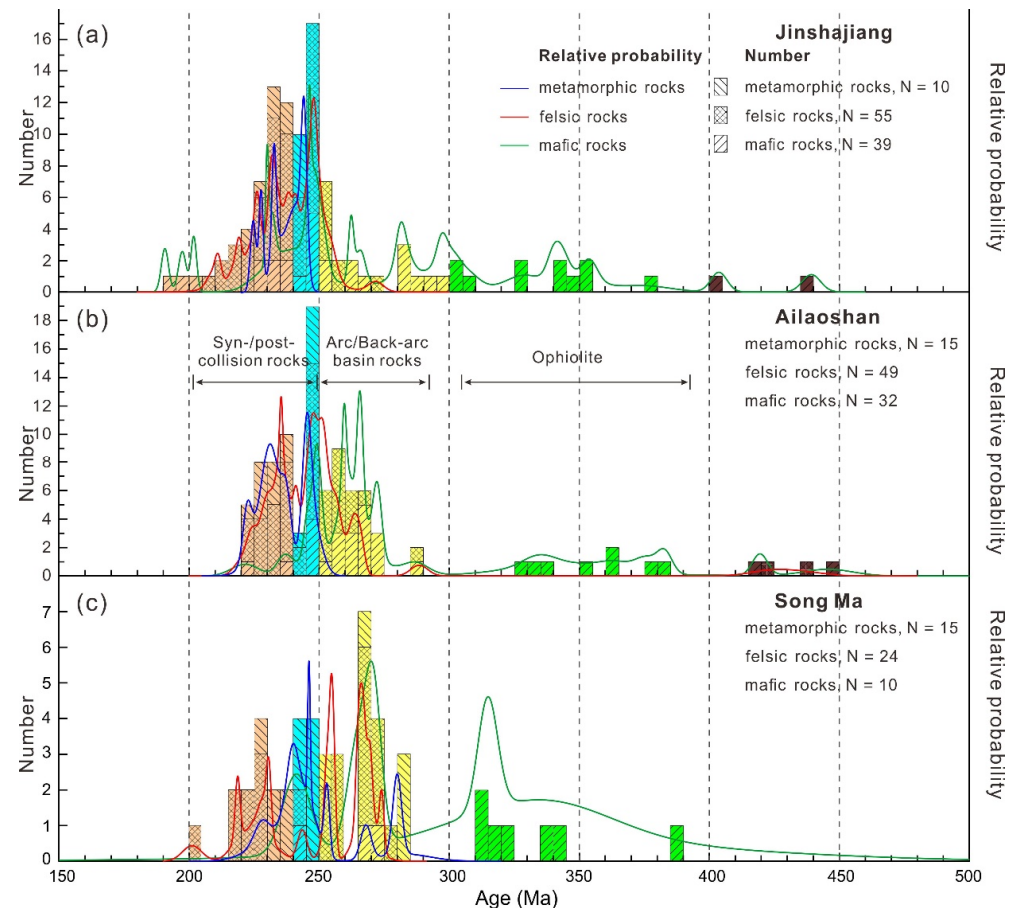


**Figure 7.** Histograms of Late Ordovician–Late Triassic crystallization and metamorphic ages in the JASB. (a) Crystallization and metamorphic ages in the Jinshajiang orogenic belt; (b) Crystallization and metamorphic ages in the Ailaoshan orogenic belt; (c) Crystallization and metamorphic ages in the Song Ma orogenic belt. Detailed data sources are listed in Supplementary Tables S7 and S8.

#### 6.1.3. ~235–202 Ma Intracontinental Rifting Magmatism

Late Triassic rocks are represented by the Jomda–Weixi, Diancangshan, Taizhong, Mili, Huashiban, Xiaguan, Wana, and Truong Son granites, granodiorites, granitic gneisses, andesites, dacites, and ignimbrites, with a few mafic plutonic and volcanic rocks in the Batang, Derong, and Lvchun areas (Supplementary Table S7). In this study, we collate 48 reliable weighted mean ages, which give an age peak of ca. 235–230 Ma (Figure 7). The peak age of these samples in the Ailaoshan orogenic belt is ca. 5 Ma older than the samples in the Jinshajiang and Song Ma orogenic belts. Therefore, magmatism during this period is probably diachronous along the JASB. Notably, the products of magmatism at this stage have relatively more felsic rocks than those at the early stage, which probably implies a substantial tectonic setting transformation during this period.

#### 6.1.4. ~248–222 Ma Metamorphism

Five amphibolite- to granulite-facies metamorphic complex belts have been identified along the JASB, including the Xuelongshan, Diancangshan, and Ailaoshan metamorphic complex belts in southeastern Yunnan and the Truong Son and Day Nui Con Voi metamor-

phic complex belts in northern Vietnam (e.g., [33,34,101,102]). Some studies have reported a few records of Triassic metamorphism in these belts, which is considered to represent the closure of the JASO (e.g., [35,36,78,103]). In this study, 40 weighted mean U–Pb metamorphic ages in the JASB (Supplementary Table S8) give two major age peaks of ca. 245 Ma and ca. 231 Ma (Figure 7). Two samples (SME-04 and SM-07E) yield weighted mean ages of ca. 280–283 Ma and are interpreted as greenschist-facies ocean floor metamorphic ages in the Song Ma orogenic belt [55]. However, the zircon grains from these samples are euhedral with clear oscillatory zoning, and the Th/U ratios of most zircons are greater than 0.2, suggesting that the ages from these zircon U–Pb ages are crystallization ages.

#### ~245 Ma Metamorphism (ca. 249–237 Ma)

Recently, eclogite-face metamorphism has been discovered in the Luomai area, north of Batang County [36]. The zircons from the (retrograde) eclogites yield weighted mean U–Pb ages of ca. 245–240 Ma, indicating an Early to Middle Triassic metamorphic event. In contrast, such metamorphic events probably also occurred in the Ailaoshan and Song Ma orogenic belts (e.g., Yuanjiang, Yaoshan, Menghao in the Ailaoshan and Chieng Khuong, Song Ca in the Song Ma), which is evidenced by the HP metamorphic zircon U–Pb ages and muscovite and biotite Ar–Ar ages (ca. 249–239 Ma) from garnet–biotite gneisses, garnet schists, amphibolites, and metagranites [33,76,78]. This evidence suggests that the JASB has experienced a HP metamorphic event during the Middle Triassic.

#### ~231 Ma Metamorphism (ca. 236–222 Ma)

The medium-pressure (MP) metamorphism of this period has been reported in the Dali, Yuanjiang, and Xinping areas from the Ailaoshan orogenic belt; and the Dien Bien Phu and Nam Co areas from the Song Ma orogenic belt [55,78,104]. Our geothermobarometers suggests that coexisting meta-mafic rocks (amphibolite) from Jinshajiang orogenic belt record similar peak *P*–*T* conditions of 591–730 °C/5.1–7.0 kbar, and thus experienced the same transitional MP amphibolite facies metamorphism. In the Dien Bien Phu and Nam Co areas, the biotite Ar–Ar ages from fine-grained paragneiss and zircon U–Pb ages from garnet hornblende yield ca. 229–228 Ma (Supplementary Table S8). In contrast, similar metamorphic records also occurred in the Yuanjiang area with a period of ca. 234–222 Ma and in the Batang area with a period of ca. 233–225 Ma (Supplementary Table S8). These ages give a period of ca. 236–222 Ma with an age peak of ca. 231 Ma (Figure 7), indicating that the rocks have experienced a MP metamorphic process during the Late Triassic.

## 6.2. Petrogenesis and Tectonic Setting

### 6.2.1. Early Permian to Early Triassic Continuous Subduction (ca. 288–249 Ma)

We found some E-MORB-like mafic rock samples (Group 1) in the Batang area. These mafic rocks yield weighted mean zircon U–Pb ages of ca. 266–262 Ma and positive  $\epsilon\text{Nd}(t)$  (+6.95) and zircon in situ  $\epsilon\text{Hf}(t)$  (+14.54 to +16.80) values (Supplementary Tables S3 and S4). They plot near the N-MORB site, similar to the Jinshajiang ophiolite (JSO), in the La/Nb vs.  $\epsilon\text{Nd}(t)$  diagram (Figure 8b) with depleted mantle-like  $\epsilon\text{Hf}(t)$  values (Figure 8c). In addition, their single-stage Hf model ages ( $T_{\text{DMI}}$ ) are similar to their zircon ages. These characters suggest a depleted mantle source for the Batang mafic rocks (Group 1). However, in comparison with typical N-MORB-like rocks, these rocks exhibit similar patterns on the island arc array in the  $\epsilon\text{Nd}(t)$  vs.  $\epsilon\text{Hf}(t)$  diagram (Figure 8a). Their Th/Yb and Ta/Yb ratios range from 0.29–0.65 and 0.22–0.28, respectively. they show a mixing trend of MORB with subduction-related materials (Figure 8b). In contrast, N-MORB-like mafic rock samples (Group 2) are collected from the northern Batang area. As previously described, these rocks have both depleted mantle and island arc basalts (IAB) geochemical characteristics (e.g., positive  $\epsilon\text{Nd}(t)$  values (+6.57 to +8.88), negative Nb and Ta anomalies, and low Nb/U, Nb/Yb, Ta/Yb, and Th/Yb ratios; Supplementary Tables S2–S4). The La/Nb vs.  $\epsilon\text{Nd}(t)$  diagram shows that the additional fluid derived from the alternative ocean crust (AOC) might play a significant role in

generating parental magma of the N-MORB-like mafic rocks. Approximately 3% to 15% of AOC-derived fluid could account for the observed  $\epsilon\text{Nd}(t)$  values and La/Nb ratios of these rocks (Figure 8b). Enrichments in LILE (e.g., Rb, Ba, and U) and depletions in HFSE (e.g., Nb and Ta) relative to N-MORB (Figure 9b) respond to aqueous fluids and melts indicated by the subducting slab. Therefore, the compositional signatures described above for Batang mafic rocks most likely indicate a back-arc basin setting, which is also supported by the ophiolite-associated mafic-ultramafic rocks in the field (Figure 2d). Additionally, the Yaxuanqiao (Group 6) mafic rocks on the western side of the Ailaoshan orogenic belt show geochemical signatures similar to those of back-arc basin basalt (BABB; [48,61]; Figure 6e,f). The La/Nb vs.  $\epsilon\text{Nd}(t)$  diagram shows that the Yaxuanqiao mafic rocks were mainly derived from the mixing of ca. 3%–7% slab fluid and depleted mantle source components (Figure 8b). However, the Maandi mafic rocks in the eastern Ailaoshan orogenic belt have relatively higher Ti contents and lower  $\epsilon\text{Nd}(t)$  values (−1.83 to +1.40; Figure 10b; Supplementary Table S3). These mafic rocks display IAB-like characteristics in the Ta/Yb vs. Th/Yb diagram (Figure 11b) and are highly affected by continental materials (Figure 8b). We considered that these rocks may have formed in an arc/back-arc basin setting and were affected by the Emeishan mantle plume and mixed with enriched mantle and crustal source components.

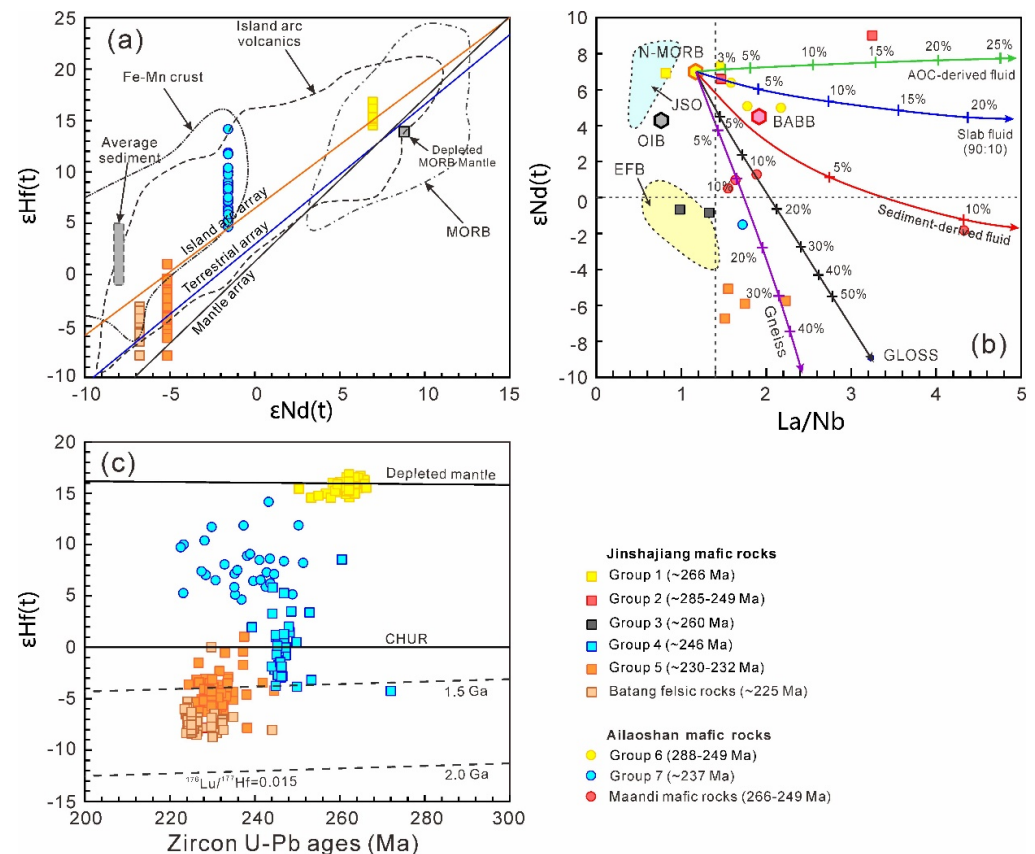


**Figure 8.** (a)  $\epsilon\text{Nd}(t)$  vs.  $\epsilon\text{Hf}(t)$  diagram, (b) La/Nb vs.  $\epsilon\text{Nd}(t)$  diagram [25], and (c) age vs.  $\epsilon\text{Hf}(t)$  diagram of the Jinshajiang and Ailaoshan mafic and felsic rocks. Data sources: The trace element contents and the average  $\epsilon\text{Nd}$  (−8) value of Global Oceanic Sediments (GLOSS) are from Plank and Langmuir [105], N-MORB are from Sun and McDonough [98] and Chauvel et al. [106], Back-arc Basin Basalts (BABB) are from Fan et al. [48], OIB are from Sun and McDonough [98] and La Flèche et al. [107], Emeishan Flood Basalts (EFB) are from Xiao et al. [108], and Jinshajiang ophiolites (JSO) are from Xu and Castillo [10]. Island arc array ( $\epsilon\text{Hf} = 1.23 \times \epsilon\text{Nd} + 6.45$ ) and mantle array ( $\epsilon\text{Hf} = 1.59 \times \epsilon\text{Nd} + 1.28$ ) are from Su [109] and Chauvel et al. [106], respectively, and Terrestrial array ( $\epsilon\text{Hf} = 1.36 \times \epsilon\text{Nd} + 2.95$ ) is from Vervoort et al. [110].

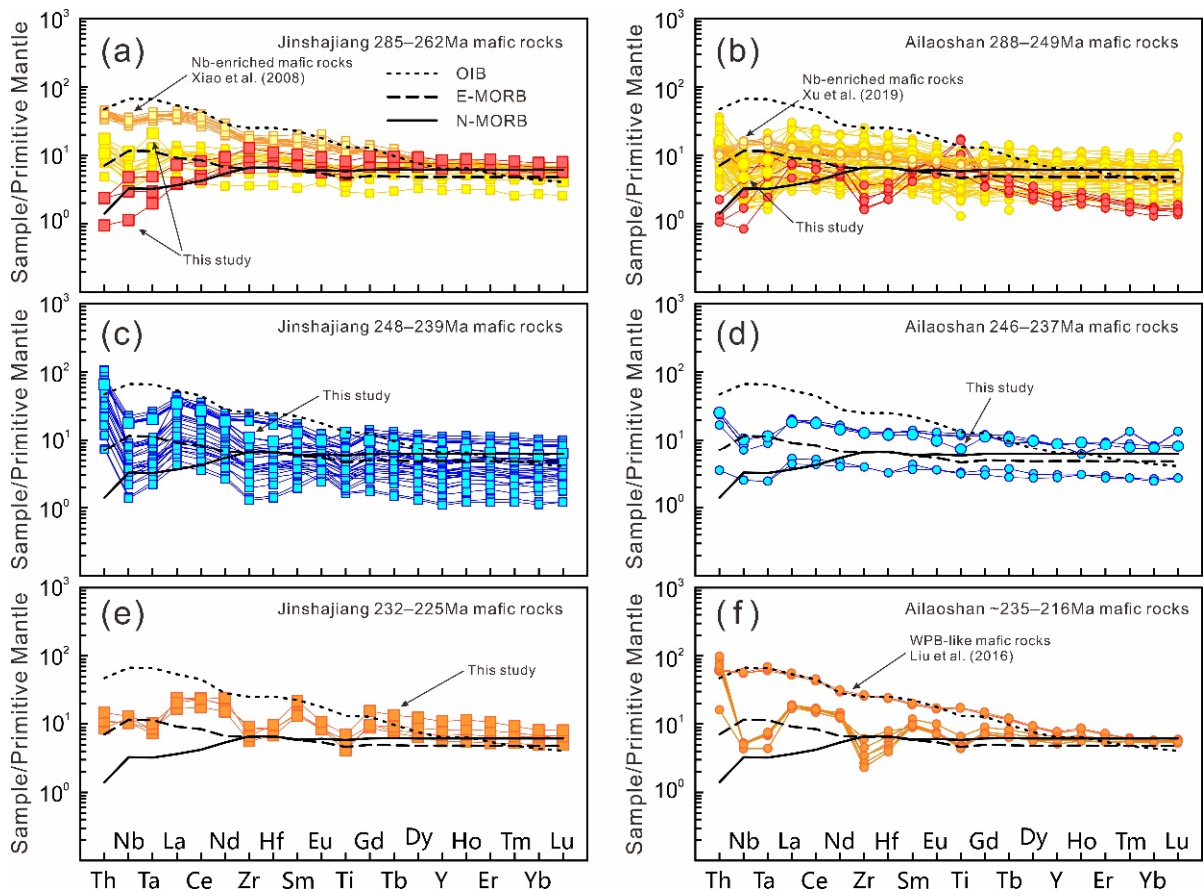


**Figure 9.** Primitive mantle-normalized incompatible element spidergrams for the Devonian-Triassic mafic rocks in the Jinshajiang and Ailaoshan orogenic belts. (a) 285–262 Ma mafic rocks in the Jinshajiang orogenic belt; (b) 288–249 Ma mafic rocks in the Ailaoshan orogenic belt [112]; (c) 248–239 Ma mafic rocks in the Jinshajiang orogenic belt [108]; (d) 246–237 Ma mafic rocks in the Ailaoshan orogenic belt; (e) 232–225 Ma mafic rocks in the Jinshajiang orogenic belt; (f) 235–216 Ma mafic rocks in the Ailaoshan orogenic belt; Detailed data sources are listed in Supplementary Table S10 [61]. The legends are the same as those in Figures 5 and 10.

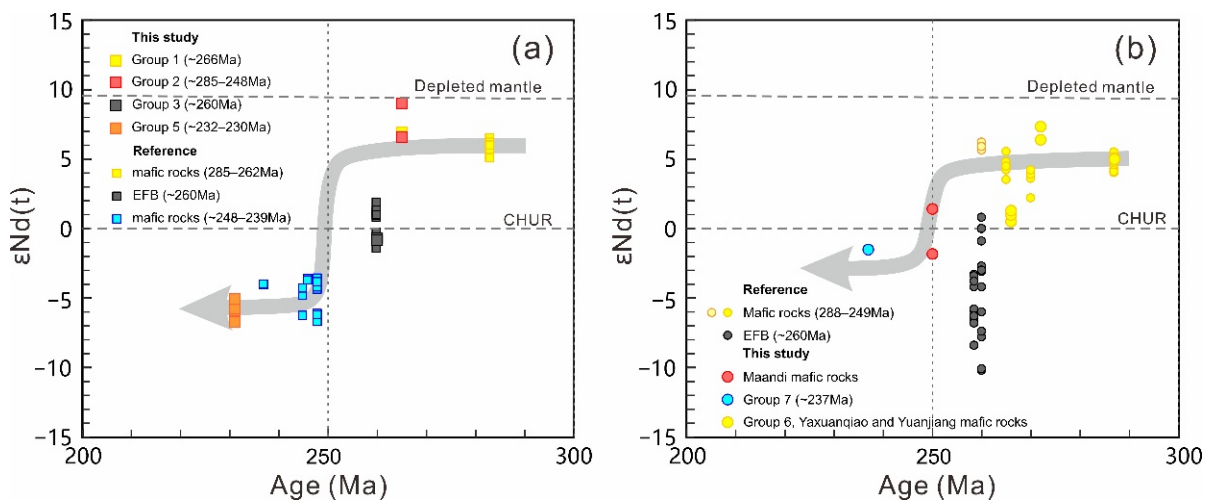


**Figure 10.** Age vs.  $\epsilon Nd(t)$  diagrams of the Jinshajiang and Ailaoshan mafic rocks. (a) Mafic rocks in the Jinshajiang orogenic belt; (b) Mafic rocks in the Ailaoshan orogenic belt. Detailed data sources are listed in Supplementary Table S9.

As mentioned in Section 6.1.1, Early Permian to Early Triassic volcanic magmatism is widespread in the JYTA. Hu et al. [111] reported that the Early Permian mafic rocks in the Baimaxueshan area consist of gabbros and basaltic–andesitic lavas, which have an arc affinity with depleted Nb, Ta, Zr, Hf, and Ti contents, and positive  $\epsilon\text{Nd}(t)$  values of +5.1 to +6.5 (Figure 10a). In contrast, similar geochemical magmatism in the Early Permian (ca. 288–272 Ma) has been reported in the Yaxuanqiao areas in the Ailaoshan orogenic belt [48] and the Dien Bien and Chieng Khuong complexes in the Song Ma orogenic belt [39], suggesting that plate subduction-associated magmatism commenced west of the JASB in the Early Permian. Subsequently, continuous subduction led to the formation of Middle Permian BABB-like rocks (e.g., Dalongkai mafic–ultral mafic rocks; [19,61]). Some studies considered that this stage of rocks with BABB-like geochemical characteristics was generated by westward subduction of the JASO (e.g., [24,39,50]). However, Middle Permian–Early Triassic subduction-associated mafic rocks (ca. 272–249 Ma) are also found in the Taizhong, Yuanjiang, Maandi, and Day Nui Con Voi areas in the eastern Ailaoshan orogenic belt [112,113], indicating eastward subduction of the Ailaoshan Paleo-Tethyan Ocean during the Middle Permian and continuing until the Early Triassic. Therefore, there are still some controversies about the subduction direction of the JASO. Based on our statistics, arc-affinity mafic rocks exposed in the JASB were formed at 288–249 Ma. Most of these mafic rocks have E-MORB-like geochemical signatures and are generally characterized by Nb and Ta depletion, LILE and HFSE enrichment (Figure 9a,b), and positive  $\epsilon\text{Nd}(t)$  values (0 to +9; Figure 10). They are typical arc/back-arc basin magmatic rocks formed in a continental arc/back-arc basin setting [5,19,48]. However, the variable mafic rock types suggest that the magma source was constantly changing from the Early to Late Permian. (1) During the Early Permian (ca. 288–272 Ma), geochemical studies of the Early Permian mafic rocks in the JYTB demonstrate that they are enriched in REE, LREE, and LILE, depleted in HFSE (Nb, Ta, and Ti), which is similar to island arc magmatic rocks with E-MORB-like REE and trace element normalized patterns. The higher Ta/Yb, Th/Yb, and Ce/Yb ratios indicate that they belong to the calc-alkaline series and formed in a continental margin arc [19,48,114]. (2) Subsequently (ca. 265–260 Ma), the Middle Permian mafic rocks in the Batang area and Yaxuanqiao volcanic arc have relatively lower REE contents, are lightly enriched in LREE and are depleted in Nb, Ta, and Ti contents. The lower Ta/Yb and Ce/Yb ratios indicate that they belong to the tholeiitic series (Figure 5b). Some mafic rocks display both depleted mantle and IAB features with N-MORB-like REE normalized patterns (Figure 9a,b), positive  $\epsilon\text{Nd}(t)$  values and relatively lower Ta/Yb, Th/Yb and La/Nb ratios (Figure 11a,b), suggesting that they are the product of partial melting of mantle wedge in a subducted environment. In addition, the basalts at this stage show pillow structures (Figure 2f), indicating that they were generated in a marine environment. Therefore, the Middle Permian mafic rocks transition from calc-alkaline series to tholeiitic series and from E-MORB type to N-MORB type, it seems reasonable to conclude that the tectonic setting may have gradually changed from the continental margin arc to the back-arc basin setting in response to the continuous westward subduction of the JASO. (3) During the Middle Permian–Early Triassic (ca. 272–249 Ma), the Mengqiao–Maandi mafic rocks from western side of the Ailaoshan orogenic belt have similar zircon U–Pb ages (or inherited zircon U–Pb ages), trace element ratios (e.g., Ti/Y) and Sm–Nd isotopes to those of Emeishan flood basalts (EFB) and show E-MORB-like REE and trace element normalized patterns and obviously depleted Nb and Ta elements [113]. Additionally, Taizhong Nb-enriched mafic rocks have high Nb and Nb/La, positive Nb and Ta anomalies, and relatively lower  $\epsilon\text{Nd}(t)$  and zircon  $\delta^{18}\text{O}$  values than N-MORB-like mafic rocks [112]. Many of them display WPB-like geochemical characteristics in the Zr vs. Zr/Y diagram (Figure 11c,d). These phenomena indicate that these mafic rocks may have been generated by the mixing of MORB-like components and Emeishan mantle plume material in the subduction zone [112]. However, it is unlikely that these Nb-enriched or high-Ti mafic rocks were formed during the westward subduction of the JASO, as the physical barrier of the

subducted plate made it difficult for mantle plume material on the eastern side of the plate to mix with mantle wedge magma on the western side of the plate. We thus propose that the bipolar subduction of the JASO occurred in the Middle Permian and ended in the Early Triassic.

#### 6.2.2. A Middle Triassic Syn-Collisional Setting (ca. 248–237 Ma)

Two gabbro samples in the Batang (Group 4) and Lvchun (Group 7) areas yield weighted mean zircon U–Pb ages of  $246.2 \pm 0.6$  Ma (Figure 4f) and  $236.9 \pm 3.0$  Ma (Figure 4c), respectively. These gabbros must have been generated by a mixture of mantle melts and crustal sedimentary material, which is supported by the following evidence: (1) they have high SiO<sub>2</sub> contents and low Mg<sup>#</sup> values; (2) they have depleted Nb, Ta, Zr, and Ti contents and high Zr/Y and Th/Yb ratios (Figure 11a–d); and (3) the Batang gabbro has variable  $\epsilon\text{Hf}(t)$  values (−4.27 to +8.53; Figure 7c). However, the Lvchun gabbro has a limited negative  $\epsilon\text{Nd}(t)$  value (−1.51) and positive  $\epsilon\text{Hf}(t)$  values (+4.64 to +14.15; Supplementary Tables S3 and S4). The Lvchun gabbro shows island arc volcanic and continental crust-like characteristics in the  $\epsilon\text{Nd}(t)$  vs.  $\epsilon\text{Hf}(t)$  diagram (Figure 7a). Notably, the average Hf isotopic composition of the sediments is high ( $\epsilon\text{Hf} = +2 \pm 3$ ) relative to its Nd isotopic composition ( $\epsilon\text{Nd} = -8.9$ ), whereas the average basaltic crust has positive  $\epsilon\text{Hf}$  and  $\epsilon\text{Nd}$  (+13.9 and +8.8, respectively), identical to MORB [106]. Therefore, significant Hf–Nd decoupling and variable  $\epsilon\text{Hf}(t)$  values occur here, indicating that abundant crustal sediments are associated with the formation of these gabbros. (4) The zircon in situ single-stage Hf model ages ( $T_{\text{DM1}}$ ) of the Batang and Lvchun gabbros are clearly older than their zircon U–Pb ages (Supplementary Table S4). In addition, the La/Nb vs.  $\epsilon\text{Nd}(t)$  diagram demonstrates that the Lvchun gabbro is mixed with approximately 16% of continental gneiss material (Figure 7b). These geochemical characteristics are similar to those of the Daheishan, Jijiading, and Deqin mafic rocks [4,24,115]. Therefore, the evidence described above indicates that these mafic rocks possibly formed in an intracontinental environment during the Middle Triassic.

Wang et al. [30] reported Early Triassic mafic rocks (ca. 249 Ma) in the Jijiading and Xiaruo areas with negative  $\epsilon\text{Nd}(t)$  values and proposed subduction of the Paleo-Tethyan Ocean along the continental margin for these mafic rocks. However, Wang et al. [115] and Zi et al. [4] reported Middle Triassic basalts (ca. 246–237 Ma) in the Jijiading and Deqin areas with negative  $\epsilon\text{Nd}(t)$  values, and felsic rocks at this stage with high SiO<sub>2</sub>, low MgO, and Al-enriched characteristics. In the Ailaoshan orogenic belt, previous studies have reported numbers of Middle Triassic mafic rocks in the Yaxuanqiao and Daheishan areas [5,19,24]. These mafic rocks contain geochemical signatures similar to those of the Jijiading and Deqin mafic rocks during this period (Figure 9d), which were considered to be a bimodal volcanic suite within a continent-arc collisional setting. In fact, all these mafic rocks show consistently depleted HFSE (e.g., Nb, Ta, Zr, Hf, and Ti) contents and enriched LILE (e.g., Rb, Ba, and Th) and LREE (Figure 9c), indicating an origin from partial melting of an enriched lithospheric mantle source. Liu et al. [26] suggested that the Middle Triassic rocks (247–237 Ma) may generate by the syncollisional continental subduction. According to the results of statistical analyses, the proportion of felsic rocks is significantly higher in magmatic rocks formed in the JASB during the Middle Triassic (Figure 7), indicating that terrestrial crustal materials were extensively involved in partial melting at this stage, resulting in mafic rocks with generally negative  $\epsilon\text{Nd}(t)$  values (Figure 10a,b). In addition, Lepvrier et al. [76] reported HP metamorphic ages (ca. 246–237 Ma) of muscovite and biotite Ar–Ar ages from paragneiss, garnet-bearing schist, and elongated granite in the Truong Son belt (Figure 1b), establishing an early phase of the Indosinian orogeny. Subsequently, Liu et al. [33] reported ca. 249–230 Ma HP metamorphic zircons in amphibolites and paragneisses, suggesting an HP metamorphic event in the Diancangshan–Ailaoshan complex during the Early–Middle Triassic. Recently, Tang et al. [36] found ca. 244–240 Ma eclogites with peak metamorphism temperature and pressure of 622–688 °C and 2.2–2.34 GPa in the Luomai

area of the Jinshajiang orogenic belt (Figure 1b) and suggested that they may represent the closure epoch of the Jinshajiang Paleo-Tethyan Ocean. All these magmatic and metamorphic records suggest that a substantial collisional event may have occurred during the Middle Triassic, which gave rise to massive orogenic magmatic rocks in the JASB (Figure 1b).

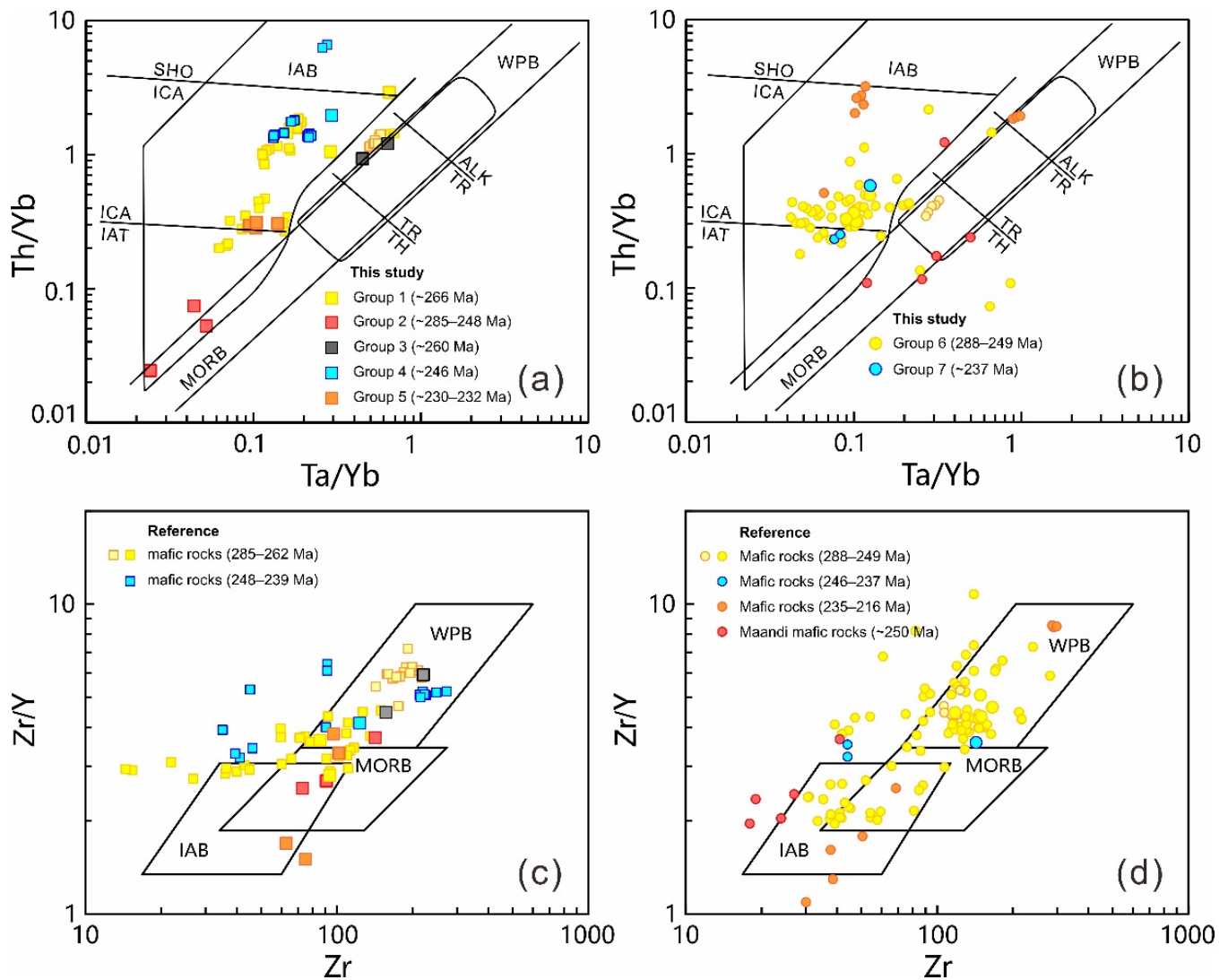


**Figure 11.** (a,b) Ta/Yb vs. Th/Yb [97] and (c,d) Zr vs. Zr/Y [116] discrimination plots for the Devonian-Triassic mafic rocks in the Jinshajiang and Ailaoshan orogenic belts. Data sources of mafic rocks are the same as those in Figure 9.

### 6.2.3. Late Triassic Postcollisional Extension (ca. 235–202 Ma)

Yang et al. [43] proposed that magmatism in the Jomda–Weixi–Yunxian volcanic arc ceased during the Late Triassic (ca. 235–210 Ma), whereas the onset of magmatism appeared in the Early Permian throughout the arc. Late Triassic (ca. 235 Ma) Taizhong amphibolite and granodiorite in the northern DAMB are characterized by negative Nb, Ta, Zr, and Hf anomalies (Figure 9f), and positive  $\epsilon\text{Nd}(t)$  and  $\epsilon\text{Hf}(t)$  values (+2.90 to +4.63 and +9.9 to +14.1, respectively) suggested that these rocks were derived from depleted mantle metasomatized by subducted oceanic sediments [117]. However, four amphibolite samples (Group 5) in the Batang area yield zircon U–Pb crystallization ages of  $231.7 \pm 2.4$  Ma and  $229.9 \pm 0.6$  Ma (Figure 4a,d). These samples display low  $\text{SiO}_2$  (44.42 wt.% to 46.51 wt.%), medium  $\text{K}_2\text{O}$  (0.80 wt.% to 1.09 wt.%), variable  $\text{Mg}^\#$  (39 to 57) and calc-alkaline characteristics (Figure 5b). The negative  $\epsilon\text{Nd}(t)$  (−5.14 to −6.77)

and variable  $\epsilon\text{Hf}(t)$  values (+1.01 to  $-7.90$ ) suggest that these calc-alkaline rocks have been highly contaminated by crustal components (ca. 30%; Figure 7b). However, such a high extent of assimilation of the crustal components would make it difficult to maintain their basaltic compositions. Generally, mafic lower crust-derived melts are characterized by low  $\text{Mg}^\#$  (<40) regardless of melting degrees, whereas those with  $\text{Mg}^\# > 40$  and low  $\text{SiO}_2$  contents can only be obtained with the involvement of a mantle source [118,119], indicating that the additional crustal components may originate from the mafic lower crust. In addition, the high- $\text{Mg}^\#$  sample ( $\text{Mg}^\# > 40$ ) have relatively high Nb, Ta and Nb/Th ratios (Supplementary Table S2) with no clearly negative Nb and Ta anomalies in the Primitive mantle-normalized trace element patterns (Figure 9e), indicating that the parental magma to Group 5 mafic rocks was enriched in HFSE and LREE relative to LILE. The variable  $\epsilon\text{Hf}(t)$  values and low  $\epsilon\text{Nd}(t)$  values of the Group 5 mafic rocks strongly suggest the involvement of a crustal component in their petrogenesis. Therefore, the Group 5 mafic rocks may be the result of upper crustal assimilation and mafic magmas derived from partial melting of a fertile mantle. Moreover, the felsic vein, which has a crystallization age of  $227.1 \pm 1.1$  Ma (Figure 3g) and  $\epsilon\text{Hf}(t)$  values ( $-5.32$  to  $-8.73$ , except for one zircon with  $-28.70$ ; Figure 7c; Supplementary Table S4) similar to those of the Batang amphibolites (Group 5), intruded into this mafic rock (Figure 2d). This phenomenon is likely evidence of bimodal magma in the Jinshajiang orogenic belt. These bimodal magmatic rocks in the Batang area may represent an extensional setting during the Late Triassic. In fact, there are four postcollisional extensional rift basins along the Jinshajiang orogenic belt, namely, the Luchun–Hongpo, the Reshuitang–Cuiyibi, the Xialaxiu–Sinda, and the Zhaokalong–Jomda basins. The former two basins, where the Batang area is located, are characterized by bimodal basalt–rhyolite and bathyal turbidite and arenaceous–politic flysch [59]. Additionally, the Late Triassic Taizhong amphibolites in the DAMB have trace element patterns similar to those of the Batang amphibolites (Group 5; Figure 9e,f). Their single-stage and two-stage Hf model ages ( $T_{\text{DM1}}$  and  $T_{\text{DM2}}$ ) are clearly older than the zircon U–Pb ages [117], indicating that crustal contamination was influential in the magmatic evolution [120]. These rocks with MORB-like isotopic compositions were likely formed by partial melting of the overriding lithosphere under decompression and thermal erosion of the upwelling asthenospheric mantle in a postcollisional extensional setting [121]. The MP metamorphic condition of this period further suggest that it was a stage of extensional setting following collisional orogeny. The crustal extension in the orogenic belt may be due to mountain root delamination [122] or breaking-off of the subducting slab [121] underneath the orogenic belt. Both processes would cause upwelling of the asthenosphere, resulting in lithospheric thinning and heating of the lower crust and then facilitating crustal uplift and extension. This tectonothermal event may also have contributed to the Late Triassic magmatism in the Youjiang Basin, southwestern China [123,124].

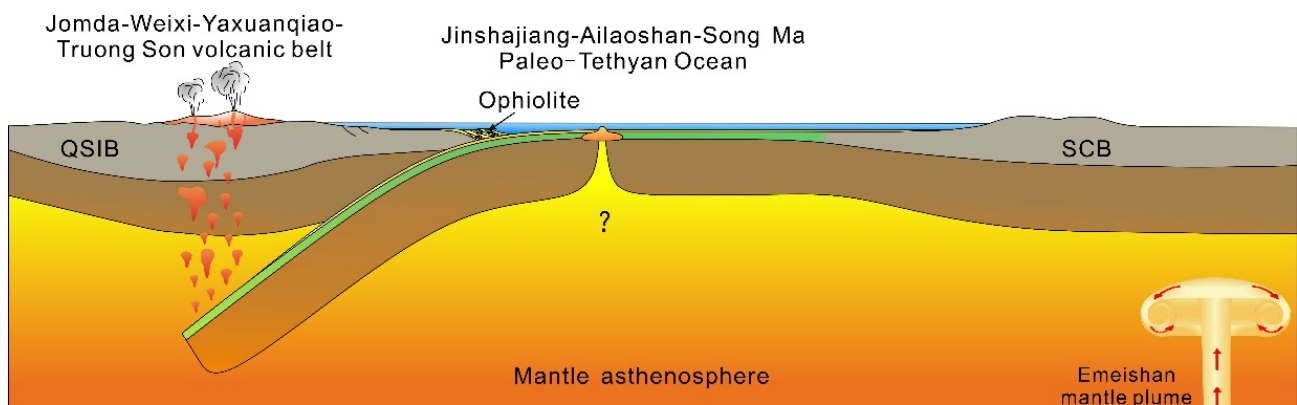
### 6.3. Geodynamic Model for the Evolution History of the JASB

The Paleo-Tethyan geodynamic evolution of the JASB has been debated for decades [9,38,51,125,126], especially the processes of subduction and closure of the JASO, which complicate our understanding of the tectonic history of the Eastern Paleo-Tethyan Ocean (e.g., [10,22,25,44,59]). Some researchers believe that the JASO evolved continuously from the Ordovician to Triassic and underwent the following stages: (1) continental rift during the Late Ordovician–Early Devonian (e.g., [11,19]); (2) ocean ridge expansion during the middle Devonian to late Carboniferous (e.g., [19,20,42]); (3) unidirectional subduction (e.g., [39,61,127]) or bidirectional subduction (e.g., [112,128,129]) during the Early Permian to Early Triassic; and (4) closure of the JASO and collision between the SCB and the QSIB during the Early to Middle Triassic (e.g., [4,19,24,78,130]). However, Xu et al. [131] suggested that there was a long-lived ocean in the northern QSIB during the Late Neoproterozoic to Late Carboniferous. Subsequently, a short period of collision

occurred between the NQB and the SCB in the Late Carboniferous, indicating that the northern segment of JASO closed during this period.

By integrating previously available geological data and the findings of our study, especially magmatic and metamorphic data from the JASB, the Early Permian to Late Triassic tectonic evolution of the JASB is reconstructed in Figure 12 and outlined below. During the Early Permian period (ca. 288–272 Ma), the JASO subducted westward under the QSIB and formed a continental margin arc along the JYTA (Figure 12a). Subsequently (ca. 272–265 Ma), continuous subduction and slab rollback resulted in overriding plate extension to open a back-arc basin in the Batang-Yaxuanqiao area and to form Middle Permian MORB-like magmatic rocks. Meanwhile, subduction-associated magmatism that resulted from the eastward subduction of the JASO may have occurred on the southwestern margin of the SCB. Therefore, bipolar subduction of the Ailaoshan–Song Ma Paleo-Tethys Ocean possibly occurred in the Middle Permian and ended in the Early Triassic (Figure 12b). In the Middle Triassic (ca. 248–237 Ma), the collision between the QSIB and SCB closed the JASO and produced an intense orogenic magma and associated HP metamorphic rocks (e.g., eclogite) in the JASB (Figure 11c). Finally, the postcollisional extension along the JASB led to the MP metamorphic event and bimodal magmatism during the Late Triassic (ca. 235–202 Ma; Figure 12d).

### (a) Early Permian (ca. 288–272 Ma)



### (b) Middle Permian-Early Triassic (ca. 272–249 Ma)

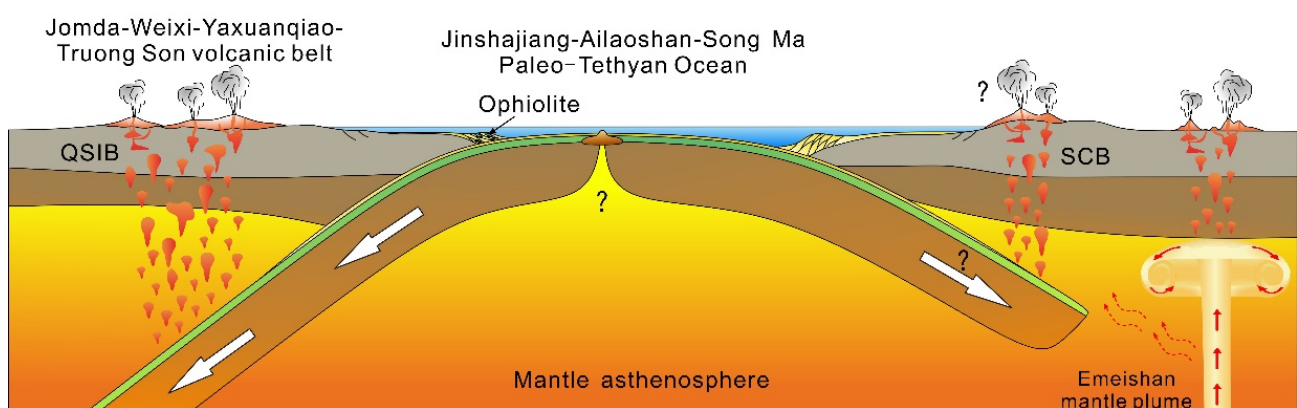
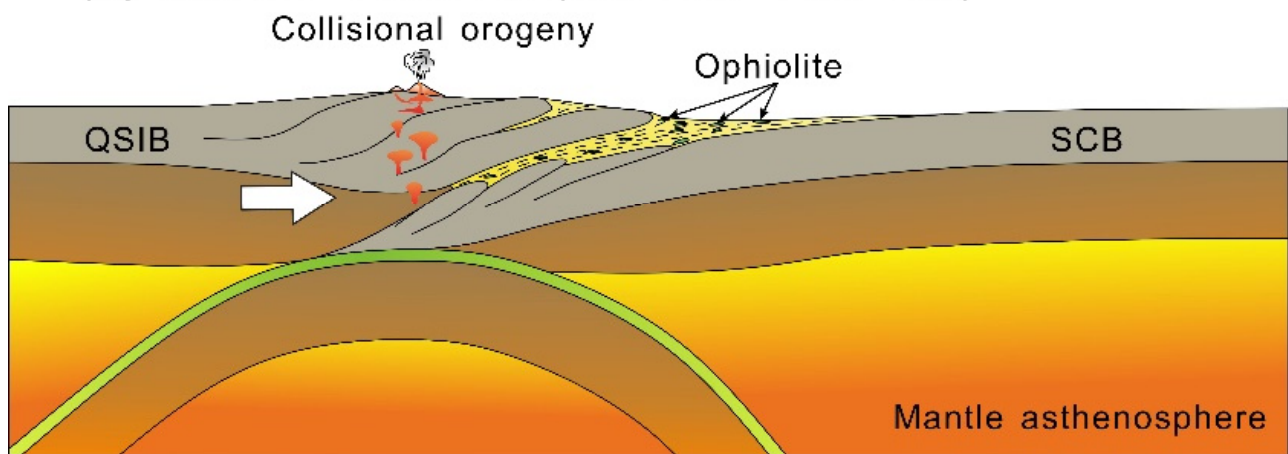
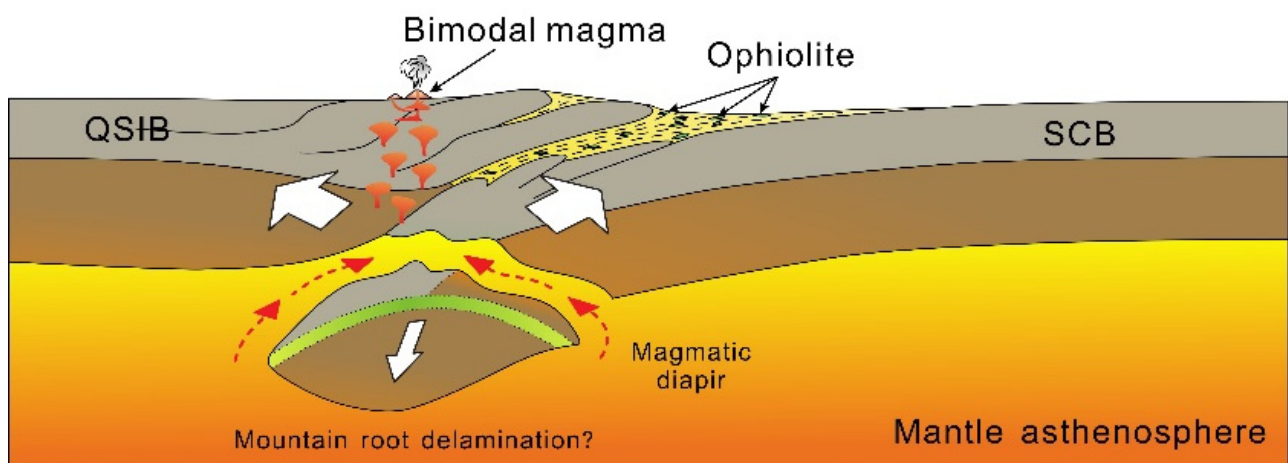


Figure 12. Cont.

## (c) Middle Triassic (ca. 248–237 Ma)



## (d) Late Triassic (ca. 235–202 Ma)



**Figure 12.** Schematic model illustrating the development of the JASB during the Early Permian to Late Triassic. (a) During the Early Permian period (ca. 288–272 Ma), the JASO subducted westward under the QSIB and formed a continental margin arc along the JYTA; (b) During Middle Permian to Early Triassic (ca. 272–265 Ma), continuous subduction and slab rollback resulted in overriding plate extension to open a back-arc basin in the Batang-Yaxuanqiao area and to form Middle Permian MORB-like magmatic rocks. Meanwhile, subduction-associated magmatism that resulted from the eastward subduction of the JASO may have occurred on the southwestern margin of the SCB. (c) During the Middle Triassic (ca. 248–237 Ma), the collision between the QSIB and SCB closed the JASO and produced an intense orogenic magma in the JASB; (d) During the Late Triassic (ca. 235–202 Ma), the postcollisional extension along the JASB led to the MP metamorphic event and bi-modal magmatism.

## 7. Conclusions

Based on an integration of geochronological, geochemical, and isotopic studies of the JASB, we obtain the following conclusions.

The Batang E-MORB- and N-MORB-like mafic rocks (Group 1 and Group 2) yield zircon U–Pb ages of  $265.8 \pm 1.9$  Ma and  $262.2 \pm 1.0$  Ma. Their  $\epsilon_{\text{Nd}}(t)$  and  $\epsilon_{\text{Hf}}(t)$  values show typical island arc arrays. These Early Permian to Early Triassic arc/back-arc basin rocks (ca. 288–248 Ma), widely exposed on both sides of the JASB, suggest that subduction of the JASO commenced in the Early Permian and bipolar subduction occurred during the

Middle Permian to Early Triassic. This study proposes that the westward subduction of the JASO is about 16 Ma earlier than eastward subduction.

The Batang (Group 4) and Lvchun Gabbros (Group 7) yield zircon U–Pb ages of  $246.2 \pm 0.6$  Ma to  $236.9 \pm 3.0$  Ma with high SiO<sub>2</sub> contents and low Mg<sup>#</sup> values. These rocks show similar  $\epsilon\text{Nd}(t)$  and  $\epsilon\text{Hf}(t)$  values to continental crust. Based on these findings and previous studies, we propose that the closure of the JASO occurred in the Middle Triassic (ca. 248–237 Ma), involving the collision between the SCB and the QSIB, and leading to syncollisional continental subduction.

The Late Triassic Batang mafic (Group 5) and felsic rocks are bimodal magmas with zircon U–Pb ages of  $231.7 \pm 2.4$  Ma to  $227.1 \pm 1.1$  Ma. These mafic rocks have negative  $\epsilon\text{Nd}(t)$  and  $\epsilon\text{Hf}(t)$  values, and show terrestrial array characteristics. The results of the  $\epsilon\text{Nd}(t)$  values and La/Nb ratios simulations indicate that approximately 30% of crustal components account for the generation of these rocks. These characteristics suggest that these rocks were probably the result of magma diapirs in a postcollisional extensional setting during the Late Triassic. Our data precisely constrain the Paleo-Tethyan orogenic process on the southwest SCB. This probably represents one of the best examples of ocean-continent transition following bipolar subduction.

**Supplementary Materials:** The following supporting information can be downloaded at: <https://www.mdpi.com/article/10.3390/min12050633/s1>, Table S1: Chemical compositions of principal minerals and metamorphic *P-T* conditions of metamafic rocks from the JASB. Table S2: Major oxides and trace elements compositions of mafic rocks from the JASB; Table S3: Sm–Nd isotopic compositions of mafic rocks from the JASB; Table S4: Hf isopleth compositions of mafic rocks from the JASB; Table S5: SHRIMP zircon U–Pb data of mafic rocks from the JASB; Table S6: LA-ICP-MS zircon U–Pb data mafic and felsic rocks from the JASB; Table S7: Summary of geochronological data on Ordovician–Triassic magmatic rocks in the JASB; Table S8: Summary of Permian–Triassic metamorphic ages in the JASB; Table S9: Summary of Sr–Nd isopleth composition of mafic rocks from the JASB; Table S10: Summary of trace elements compositions of mafic rocks from the JASB.

**Author Contributions:** Conceptualization, W.X. (Wentao Xu) and F.L.; methodology, W.X. (Wentao Xu); validation, F.L. and W.X. (Wang Xu); investigation, W.X. (Wentao Xu), F.L., L.J., H.W., F.W. and D.W.; resources, F.L.; writing—original draft preparation, W.X. (Wentao Xu); writing—review and editing, W.X. (Wentao Xu) and H.W.; project administration, F.L.; funding acquisition, F.L. All authors have read and agreed to the published version of the manuscript.

**Funding:** This research was funded by the National Natural Science Foundation of China, grant number 91855206, 40725007, and the Foundation of the Key Laboratory of Deep-Earth Dynamics of Ministry of Natural Resources, grant number J1901-20-2.

**Data Availability Statement:** Data are contained within the supplementary materials.

**Conflicts of Interest:** The authors declare no conflict of interest.

## References

1. Şengör, A.M.C. The evolution of Paleo-Tethys in the Tibetan segment of the Alpides. *Geol. Ecol. Stud. Qinghai-Xizang Plateau* **1981**, *1*, 51–56.
2. Şengör, A.M.C. Tectonics of the Tethysides: Orogenic Collage Development in a Collisional Setting. *Annu. Rev. Earth Planet Sci.* **1987**, *15*, 213–244. [[CrossRef](#)]
3. Zhong, D.L.; Zhao, J. The Changning–Menglian tectonic belt. In *Paleotethysides in West Yunnan and Sichuan, China*; Zhong, D.L., Ed.; Science Press: Beijing, China, 2000; pp. 112–123. (In Chinese)
4. Zi, J.W.; Cawood, P.A.; Fan, W.M.; Wang, Y.J.; Tohver, E.; McCuaig, T.C.; Peng, T.P. Triassic collision in the Paleo-Tethys Ocean constrained by volcanic activity in SW China. *Lithos* **2012**, *144–145*, 145–160. [[CrossRef](#)]
5. Jian, P.; Liu, D.Y.; Kröner, A.; Zhang, Q.; Wang, Y.Z.; Sun, X.M.; Zhang, W. Devonian to Permian plate tectonic cycle of the Paleo-Tethys Orogen in southwest China (I): Geochemistry of ophiolites, arc/back-arc assemblages and within-plate igneous rocks. *Lithos* **2009**, *113*, 748–766. [[CrossRef](#)]

6. Nakano, N.; Osanai, Y.; Minh, N.T.; Miyamoto, T.; Hayasaka, Y.; Owada, M. Discovery of high-pressure granulite-facies metamorphism in northern Vietnam: Constraints on the Permo-Triassic Indochinese continental collision tectonics. *Comptes Rendus Géosci.* **2008**, *340*, 127–138. [[CrossRef](#)]
7. Vương, N.V.; Hansen, B.T.; Wemmer, K.; Lepvrier, C.; Tích, V.V.; Thắng, T.T. U/Pb and Sm/Nd dating on ophiolitic rocks of the Song Ma suture zone (northern Vietnam): Evidence for upper paleozoic paleotethyan lithospheric remnants. *J. Geodyn.* **2013**, *69*, 140–147. [[CrossRef](#)]
8. Wang, C.M.; Bagas, L.; Lu, Y.J.; Santosh, M.; Du, B.; McCuaig, T.C. Terrane boundary and spatio-temporal distribution of ore deposits in the Sanjiang Tethyan Orogen: Insights from zircon Hf-isotopic mapping. *Earth-Sci. Rev.* **2016**, *156*, 39–65. [[CrossRef](#)]
9. Wang, Y.J.; Qian, X.; Cawood, P.A.; Liu, H.C.; Feng, Q.; Zhao, G.C.; Zhang, Y.H.; He, H.Y.; Zhang, P.Z. Closure of the East Paleotethyan Ocean and amalgamation of the Eastern Cimmerian and Southeast Asia continental fragments. *Earth-Sci. Rev.* **2018**, *186*, 195–230. [[CrossRef](#)]
10. Xu, J.F.; Castillo, P.R. Geochemical and Nd–Pb isotopic characteristics of the Tethyan asthenosphere: Implications for the origin of the Indian Ocean mantle domain. *Tectonophysics* **2004**, *393*, 9–27. [[CrossRef](#)]
11. Liu, H.C.; Xia, X.P.; Lai, C.K.; Gan, C.S.; Zhou, Y.Z.; Huangfu, P.P. Break-away of South China from Gondwana: Insights from the Silurian high-Nb basalts and associated magmatic rocks in the Diancangshan-Ailaoshan fold belt (SW China). *Lithos* **2018**, *318*, 194–208. [[CrossRef](#)]
12. Wang, D.B.; Wang, L.Q.; Yin, F.G.; Sun, Z.M.; Wang, B.D.; Zhang, W.P. Timing and nature of the Jinshajiang Paleotethys: Constraints from zircon U–Pb age and Hf isotope of the Dongzhulin layered gabbro from Jinshajiang ophiolite belt, northwestern Yunnan. *Acta Petrol. Sin.* **2012**, *28*, 1542–1550, (In Chinese with English abstract).
13. Xu, J.; Xia, X.P.; Huang, C.; Cai, K.D.; Yin, C.Q.; Lai, C.K. Changes of provenance of Permian and Triassic sedimentary rocks from the Ailaoshan suture zone (SW China) with implications for the closure of the eastern Paleotethys. *J. Asian Earth Sci.* **2019**, *170*, 234–248. [[CrossRef](#)]
14. Xu, J.; Xia, X.P.; Lai, C.K.; Long, X.P.; Huang, C. When Did the Paleotethys Ailaoshan Ocean Close: New Insights from Detrital Zircon U–Pb age and Hf Isotopes. *Tectonics* **2019**, *38*, 1798–1823. [[CrossRef](#)]
15. Wilson, J.T. Did the Atlantic Close and then Re-Open? *Nature* **1966**, *211*, 676–681. [[CrossRef](#)]
16. Pearce, J.A.; Cann, J.R. Tectonic setting of basic volcanic rocks determined using trace element analyses. *Earth Planet. Sci. Lett.* **1973**, *19*, 290–300. [[CrossRef](#)]
17. Polat, A.; Appel, P.W.U.; Fryer, B.J. An overview of the geochemistry of Eoarchean to Mesoarchean ultramafic to mafic volcanic rocks, SW Greenland: Implications for mantle depletion and petrogenetic processes at subduction zones in the early Earth. *Gondwana Res.* **2011**, *20*, 255–283. [[CrossRef](#)]
18. Thakurta, J.; Ripley, E.M.; Li, C. Geochemical constraints on the origin of sulfide mineralization in the Duke Island Complex, southeastern Alaska. *Geochem. Geophys. Geosyst.* **2013**, *9*, Q07003. [[CrossRef](#)]
19. Jian, P.; Liu, D.Y.; Kröner, A.; Zhang, Q.; Wang, Y.Z.; Sun, X.M.; Zhang, W. Devonian to Permian plate tectonic cycle of the Paleo-Tethys Orogen in southwest China (II): Insights from zircon ages of ophiolites, arc/back-arc assemblages and within-plate igneous rocks and generation of the Emeishan CFB province. *Lithos* **2009**, *113*, 767–784. [[CrossRef](#)]
20. Hu, W.J.; Zhong, H.; Zhu, W.G.; He, X.H. Elemental and Sr–Nd isotopic geochemistry of the basalts and microgabbros in the Shuanggou ophiolite, SW China: Implication for the evolution of the Palaeotethys Ocean. *Geol. Mag.* **2015**, *152*, 210–224. [[CrossRef](#)]
21. Hu, W.J.; Zhong, H.; Chu, Z.Y.; Zhu, W.G.; Bai, Z.J.; Zhang, C. Ancient refertilization process preserved in the plagioclase peridotites: An example from the Shuanggou ophiolite, southwest China. *J. Geophys. Res. Solid Earth* **2019**, *125*, e2019JB017552. [[CrossRef](#)]
22. Wang, X.F.; Metcalfe, I.; Jian, P.; He, L.Q.; Wang, C.S. The Jinshajiang-Ailaoshan Suture Zone, China: Tectonostratigraphy, age and evolution. *J. Asian Earth Sci.* **2000**, *18*, 675–690. [[CrossRef](#)]
23. Yumul, G.P.; Zhou, M.F.; Wang, C.Y.; Zhao, T.P.; Dimalanta, C.B. Geology and geochemistry of the Shuanggou ophiolite (Ailao Shan ophiolitic belt), Yunnan Province, SW China: Evidence for a slow-spreading oceanic basin origin. *J. Asian Earth Sci.* **2008**, *32*, 385–395. [[CrossRef](#)]
24. Lai, C.K.; Meffre, S.; Crawford, A.J.; Zaw, K.; Xue, C.D.; Halpin, J.A. The Western Ailaoshan Volcanic Belts and their SE Asia connection: A new tectonic model for the Eastern Indochina Block. *Gondwana Res.* **2014**, *26*, 52–74. [[CrossRef](#)]
25. Li, G.Z.; Li, C.S.; Ripley, E.M.; Kamo, S.; Su, S.G. Geochronology, petrology and geochemistry of the Nanlinshan and Banpo mafic–ultramafic intrusions: Implications for subduction initiation in the eastern Paleo-Tethys. *Contrib. Mineral. Petrol.* **2012**, *164*, 773–788. [[CrossRef](#)]
26. Liu, H.C.; Wang, Y.J.; Cawood, P.A.; Guo, X.F. Episodic slab rollback and back-arc extension in the Yunnan–Burma region: Insights from Cretaceous Nb-enriched and oceanic-island basalt-like mafic rocks. *Geol. Soc. Am. Bull.* **2017**, *129*, 698–714. [[CrossRef](#)]
27. Wang, C.Y.; Zhou, M.F.; Keays, R.R. Geochemical constraints on the origin of the Permian Baimazhai mafic–ultramafic intrusion, SW China. *Contrib. Mineral. Petrol.* **2006**, *152*, 309–321. [[CrossRef](#)]

28. Wang, C.Y.; Zhou, M.F.; Qi, L. Permian flood basalts and mafic intrusions in the Jinping (SW China) Song Da (northern Vietnam) district: Mantle sources, crustal contamination and sulfide segregation. *Chem. Geol.* **2007**, *243*, 317–343. [[CrossRef](#)]
29. Wang, J.; Wang, Q.; Zhang, C.; Dan, W.; Qi, Y.; Zhang, X.Z.; Xia, X.P. Late Permian Bimodal Volcanic Rocks in the Northern Qiangtang Terrane, Central Tibet: Evidence for Interaction Between the Emeishan Plume and the Paleo-Tethyan Subduction System. *J. Geophys. Res. Solid Earth* **2018**, *123*, 6540–6561. [[CrossRef](#)]
30. Wang, Y.N.; Xue, S.C.; Deng, J.; Wang, Q.F.; Li, C.S.; Ripley, E.M. Triassic arc mafic magmatism in North Qiangtang: Implications for tectonic reconstruction and mineral exploration. *Gondwana Res.* **2020**, *82*, 337–353. [[CrossRef](#)]
31. Xiao, L.; Xu, Y.G.; Mei, H.J.; He, B. Late Permian flood basalts at Jinping area and its relation to Emei mantle plume geochemical evidences. *Acta Petrol. Sin.* **2003**, *19*, 38–48, (In Chinese with English abstract).
32. Zhang, H.; Yang, T.; Hou, Z.; Dai, M.; Hou, K. Permian back-arc basin basalts in the Yushu area: New constrain on the Paleo-Tethyan evolution of the north-central Tibet. *Lithos* **2017**, *286–287*, 216–226. [[CrossRef](#)]
33. Liu, F.L.; Wang, F.; Liu, P.H.; Liu, C.H. Multiple metamorphic events revealed by zircons from the Diancang Shan-Ailao Shan metamorphic complex, southeastern Tibetan Plateau. *Gondwana Res.* **2013**, *24*, 429–450. [[CrossRef](#)]
34. Ji, L.; Liu, F.L.; Wang, F.; Cai, J.; Wang, W.; Tian, Z.H.; Liu, L.S. Ployphase metamorphism in Diancang Shan-Ailao Shan complex zone: Constraints from U–Pb dating and trace elements of zircons in metasedimentary rocks, Gasa area. *Acta Petrol. Sin.* **2017**, *33*, 605–621, (In Chinese with English abstract).
35. Nakano, N.; Osanai, Y.; Sajeev, K.; Hayasaka, Y.; Miyamoto, T.; Minh, N.T.; Owada, M.; Windley, B. Triassic eclogite from northern Vietnam: Inferences and geological significance. *J. Metamorph. Geol.* **2010**, *28*, 59–76. [[CrossRef](#)]
36. Tang, Y.; Qin, Y.D.; Gong, X.D.; Duan, Y.Y.; Chen, G.; Yao, H.Y.; Liao, J.X.; Liao, S.Y.; Wang, D.B.; Wang, B.D. Discovery of eclogites in Jinsha River suture zone, Gonjo County, eastern Tibet and its restriction on Paleo-Tethyan evolution. *China Geol.* **2020**, *3*, 83–103. [[CrossRef](#)]
37. Chung, S.L.; Lee, T.Y.; Lo, C.H.; Wang, P.L.; Chen, C.Y.; Yem, N.T.; Hoa, T.T.; Wu, G.Y. Intraplate extension prior to continental extrusion along the Ailao Shan-Red River shear zone. *Geology* **1997**, *25*, 311–314. [[CrossRef](#)]
38. Deng, J.; Wang, Q.F.; Li, G.J.; Santosh, M. Cenozoic tectono-magmatic and metallogenic processes in the Sanjiang region, southwestern China. *Earth-Sci. Rev.* **2014**, *138*, 268–299. [[CrossRef](#)]
39. Liu, J.L.; Tran, M.D.; Tang, Y.; Nguyen, Q.L.; Tran, T.H.; Wu, W.B.; Chen, J.F.; Zhang, Z.C.; Zhao, Z.D. Permo-Triassic granitoids in the northern part of the Truong Son belt, NW Vietnam: Geochronology, geochemistry and tectonic implications. *Gondwana Res.* **2012**, *22*, 628–644. [[CrossRef](#)]
40. Metcalfe, I. Permian tectonic framework and palaeogeography of SE Asia. *J. Asian Earth Sci.* **2002**, *20*, 551–566. [[CrossRef](#)]
41. Metcalfe, I. Gondwana dispersion and Asian accretion: Tectonic and palaeogeographic evolution of eastern Tethys. *J. Asian Earth Sci.* **2013**, *66*, 1–33. [[CrossRef](#)]
42. Trung, N.M.; Tsujimori, T.; Itaya, T. Honvang serpentinite body of the Song Ma fault zone, Northern Vietnam: A remnant of oceanic lithosphere within the Indochina–South China suture. *Gondwana Res.* **2006**, *9*, 225–230. [[CrossRef](#)]
43. Yang, T.N.; Ding, Y.; Zhang, H.R.; Fan, J.W.; Liang, M.J.; Wang, X.H. Two-phase subduction and subsequent collision defines the Paleotethyan tectonics of the southeastern Tibetan Plateau: Evidence from zircon U–Pb dating, geochemistry, and structural geology of the Sanjiang orogenic belt, southwest China. *Geol. Soc. Am. Bull.* **2014**, *126*, 1654–1682. [[CrossRef](#)]
44. Yang, T.N.; Xue, C.D.; Xin, D.; Liang, M.J.; Liao, C. Paleotethyan tectonic evolution of the Sanjiang Orogenic Belt, SW China: Temporal and spatial distribution pattern of arc-like igneous rocks. *Acta Petrol. Sin.* **2019**, *35*, 1324–1340. [[CrossRef](#)]
45. Metcalfe, I. Gondwanaland dispersion, Asian accretion and evolution of eastern Tethys\*. *J. Geol. Soc. Aust.* **1996**, *43*, 605–623. [[CrossRef](#)]
46. Metcalfe, I. Paleozoic and Mesozoic geological evolution of the SE Asian region: Multidisciplinary constrains and implication for biogeography. In *Biogeography and Geological Evolution of SE Asia*; Backhuys Publishers: Leiden, The Netherlands, 1998.
47. Metcalfe, I. Palaeozoic and Mesozoic tectonic evolution and palaeogeography of East Asian crustal fragments: The Korean Peninsula in context. *Gondwana Res.* **2006**, *9*, 24–46. [[CrossRef](#)]
48. Fan, W.M.; Wang, Y.J.; Zhang, A.M.; Zhang, F.F.; Zhang, Y.Z. Permian arc–back-arc basin development along the Ailaoshan tectonic zone: Geochemical, isotopic and geochronological evidence from the Mojiang volcanic rocks, Southwest China. *Lithos* **2010**, *119*, 553–568. [[CrossRef](#)]
49. Jian, P.; Liu, D.Y.; Sun, X.M. SHRIMP dating of the Permo-Carboniferous Jinshajiang ophiolite, southwestern China: Geochronological constraints for the evolution of Paleo-Tethys. *J. Asian Earth Sci.* **2008**, *32*, 371–384. [[CrossRef](#)]
50. Zi, J.W.; Cawood, P.A.; Fan, W.M.; Wang, Y.J.; Tohver, E. Contrasting rift and subduction-related plagiogranites in the Jinshajiang ophiolitic mélange, southwest China, and implications for the Paleo-Tethys. *Tectonics* **2012**, *31*, 1–18. [[CrossRef](#)]
51. Zhong, D.L. *The Paleotethysides in West Yunnan and Sichuan, China*; Beijing Science Press: Beijing, China, 1998; 230p. (In Chinese)
52. Zhang, Q.; Wang, C.Y.; Liu, D.; Jian, P.; Qian, Q.; Zhou, G.Q.; Robinson, P.T. A brief review of ophiolites in China. *J. Asian Earth Sci.* **2008**, *32*, 308–324. [[CrossRef](#)]
53. Jian, P.; Wang, X.F.; He, Q.L.; Wang, C.S. U–Pb zircon dating of the Shuanggou ophiolite from Xingping County, Yunnan Province. *Acta Petrol. Sin.* **1998**, *14*, 80–84, (In Chinese with English abstract).
54. Lai, C.K.; Meffre, S.; Crawford, A.J.; Zaw, K. The Central Ailaoshan ophiolite and modern analogs. *Gondwana Res.* **2014**, *26*, 75–88. [[CrossRef](#)]

55. Zhang, R.Y.; Lo, C.H.; Li, X.H.; Chung, S.L.; Anh, T.T.; Tri, T.V. U-Pb dating and tectonic implication of ophiolite and metabasite from the Song Ma suture zone, northern Vietnam. *Am. J. Sci.* **2014**, *314*, 649–678. [[CrossRef](#)]
56. Xia, X.P.; Nie, X.S.; Lai, C.K.; Wang, Y.J.; Long, X.P.; Meffre, S. Where was the Ailaoshan Ocean and when did it open: A perspective based on detrital zircon U–Pb age and Hf isotope evidence. *Gondwana Res.* **2016**, *36*, 488–502. [[CrossRef](#)]
57. Wang, Q.F.; Deng, J.; Li, C.S.; Li, G.J.; Yu, L.; Qiao, L. The boundary between the Simao and Yangtze blocks and their locations in Gondwana and Rodinia: Constraints from detrital and inherited zircons. *Gondwana Res.* **2014**, *26*, 438–448. [[CrossRef](#)]
58. Wang, X.; Qu, L.; Yan, C.; Wang, C.; Zhang, Z.; Zhu, L. Stratigraphic Division and Correlation of the Carboniferous and-Permian in Yunnan Province. *J. Stratigr.* **2018**, *42*, 461–467.
59. Hou, Z.Q.; Wang, L.Q.; Khin, Z.; Mo, X.X.; Wang, M.J.; Li, D.M.; Pan, G.T. Post-collisional crustal extension setting and VHMS mineralization in the Jinshajiang orogenic belt, southwestern China. *Ore Geol. Rev.* **2003**, *22*, 177–199. [[CrossRef](#)]
60. Mo, X.X.; Deng, J.F.; Lu, F.X. Volcanism and the evolution of Tethys in Sanjiang area, southwestern China. *J. Southeast Asian Earth Sci.* **1994**, *9*, 325–333. [[CrossRef](#)]
61. Liu, H.C.; Wang, Y.J.; Zi, J.W. Petrogenesis of the Dalongkai ultramafic-mafic intrusion and its tectonic implication for the Paleotethyan evolution along the Ailaoshan tectonic zone (SW China). *J. Asian Earth Sci.* **2017**, *141*, 112–124. [[CrossRef](#)]
62. Hou, L.; Guo, L.; Xu, S.; Zhang, Q.; Zeng, X. In situ geochemistry and Fe–O isotopic composition of iron oxides from the Pha Lek Fe deposit, northwest Truong Son orogenic belt, Laos: Implications for ore-forming processes. *Miner. Depos.* **2021**, *56*, 1405–1421. [[CrossRef](#)]
63. Hoa, T.T.; Anh, T.T.; Phuong, N.T.; Dung, P.T.; Anh, T.V.; Izokh, A.E.; Borisenko, A.S.; Lan, C.Y.; Chung, S.L.; Lo, C.H. Permo-Triassic intermediate felsic magmatism of the Truong Son belt, eastern margin of Indochina. *Comptes Rendus Géosci.* **2008**, *340*, 112–126. [[CrossRef](#)]
64. Kamvong, T.; Zaw, K.; Meffre, S.; Maas, R.; Stein, H.; Lai, C.-K. Adakites in the Truong Son and Loei fold belts, Thailand and Laos: Genesis and implications for geodynamics and metallogeny. *Gondwana Res.* **2014**, *26*, 165–184. [[CrossRef](#)]
65. Hou, L.; Liu, S.; Guo, L.; Xiong, F.; Li, C.; Shi, M.; Zhang, Q.; Xu, S.; Wu, S. Geology, Geochronology, and Hf Isotopic Composition of the Pha Lek Fe Deposit, Northern Laos: Implications for Early Permian Subduction-Related Skarn Fe Mineralization in the Truong Son Belt. *J. Earth Sci.* **2019**, *30*, 109–120. [[CrossRef](#)]
66. Hou, L.; Xiong, F.; Wang, W.; Guo, L.; Peng, H.; Ni, S.; Zhang, Q. Carboniferous-Triassic felsic igneous rocks and typical mineral deposits in the Truong Son orogenic belt, SE Asia: Implications for Paleo-Tethyan tectonic evolution and metallogeny. *Ore Geol. Rev.* **2019**, *112*, 103036. [[CrossRef](#)]
67. Yunnan Bureau of Geology and Mineral Resources (Yunnan BGMR). *Regional Geology of Yunnan Province*; Beijing Geology Publications House: Beijing, China, 1990; pp. 273–428. (In Chinese)
68. Liu, J.L.; Wang, A.J.; Cao, S.Y.; Zou, Y.X.; Tang, Y.; Chen, Y. Geochronology and tectonic implication of migmatites from Diancangshan, Western Yunnan, China. *Acta Petrol. Sin.* **2008**, *24*, 413–420. (In Chinese with English abstract)
69. Hu, J.C. Determination of the age of metamorphism of the Jinsha River metamorphic belt. *Reg. Geol. China* **1983**, *4*, 43–56. (In Chinese with English abstract)
70. Cao, W.T.; Yan, D.P.; Qiu, L.; Zhang, Y.X.; Qiu, J.W. Structural style and metamorphic conditions of the Jinshajiang metamorphic belt: Nature of the Paleo-Jinshajiang orogenic belt in the eastern Tibetan Plateau. *J. Asian Earth Sci.* **2015**, *113*, 748–765. [[CrossRef](#)]
71. Li, C.; Zhai, Q.; Dong, Y.; Huang, X. Discovery of eclogite and its geological significance in Qiangtang area, central Tibet. *Chin. Sci. Bull.* **2006**, *51*, 1095–1100. [[CrossRef](#)]
72. Leloup, P.H.; Kienast, J.R. High-temperature metamorphism in a major strike-slip shear zone: The Ailao Shan-Red River, People’s Republic of China. *Earth Planet. Sci. Lett.* **1993**, *118*, 213–234. [[CrossRef](#)]
73. Tapponnier, P.; Lacassin, R.; Leloup, P.H.; Schärer, U.; Zhong, D.L.; Wu, H.W.; Liu, X.H.; Ji, S.C.; Zhang, L.S.; Zhong, J.Y. The Ailao Shan/Red River metamorphic belt: Tertiary left-lateral shear between Indochina and South China. *Nature* **1990**, *343*, 431–437. [[CrossRef](#)]
74. Schärer, U.; Tapponnier, P.; Lacassin, R.; Leloup, P.H.; Zhong, D.; Ji, S. Intraplate tectonics in Asia: A precise age for large-scale Miocene movement along the Ailao Shan-Red River shear zone, China. *Earth Planet. Sci. Lett.* **1990**, *97*, 65–77. [[CrossRef](#)]
75. Ji, L.; Liu, F.; Wang, F.; Santosh, M.; Tian, Z.; Sun, Z. Mineral phase equilibria and zircon geochronology constrain multiple metamorphic events of high-pressure pelitic granulites in south-eastern Tibetan Plateau. *Geol. J.* **2019**, *55*, 1332–1356. [[CrossRef](#)]
76. Lepvrier, C.; Maluski, H.; Nguyen, V.V.; Roques, D.; Axente, V.; Rangin, C. Indosinian NW-trending shear zones within the Truong Son belt (Vietnam)  $^{40}\text{Ar}$ - $^{39}\text{Ar}$  Triassic ages and Cretaceous to Cenozoic overprints. *Tectonophysics* **1997**, *283*, 105–127. [[CrossRef](#)]
77. Lepvrier, C.; Maluski, H.; Tich, V.V.; Leyreloup, A.; Thi, P.T.; Nguyen, V.V. The Early Triassic Indosinian orogeny in Vietnam (Truong Son Belt and Kontum Massif); implications for the geodynamic evolution of Indochina. *Tectonophysics* **2004**, *393*, 87–118. [[CrossRef](#)]

78. Zhang, R.Y.; Lo, C.-H.; Chung, S.L.; Grove, M.; Omori, S.; Iizuka, Y.; Liou, J.G.; Tri, T.V. Origin and Tectonic Implication of Ophiolite and Eclogite in the Song Ma Suture Zone between the South China and Indochina Blocks. *J. Metamorph. Geol.* **2013**, *31*, 49–62. [[CrossRef](#)]
79. Whitney, D.L.; Evans, B.W. Abbreviations for names of rock-forming minerals. *Am. Mineral.* **2010**, *95*, 185–187. [[CrossRef](#)]
80. Hawthorne, F.C.; Oberti, R.; Harlow, G.E.; Maresch, W.V.; Martin, R.F.; Schumacher, J.C.; Welch, M.D. Nomenclature of the amphibole supergroup. *Am. Mineral.* **2012**, *97*, 2031–2048. [[CrossRef](#)]
81. Kohn, M.J.; Spear, F.S. Two new geobarometers for garnet amphibolites, with applications to southeastern Vermont. *Am. Mineral.* **1990**, *75*, 89–96.
82. Ravna, E.K. Distribution of Fe<sup>2+</sup> and Mg between coexisting garnet and hornblende in synthetic and natural systems: An empirical calibration of the garnet–hornblende Fe–Mg geothermometer. *Lithos* **2000**, *53*, 265–277. [[CrossRef](#)]
83. Wu, C.M.; Chen, H.X. Revised Ti-in-biotite geothermometer for ilmenite- or rutile-bearing crustal metapelites. *Sci. Bull.* **2015**, *60*, 116–121. [[CrossRef](#)]
84. Johnson, M.C.; Rutherford, M.J. Experimental calibration of an aluminum-in-hornblende geobarometer applicable to calc-alkaline rocks. *EOS* **1988**, *69*, 1511.
85. Sláma, J.; Kosler, J.; Condon, D.J.; Crowley, J.L.; Gerdes, A.; Hanchar, J.M.; Horstwood, M.S.A.; Morris, G.A.; Nasdala, L.; Norberg, N.; et al. Plesovice zircon—A new natural reference material for U–Pb and Hf isotopic microanalysis. *Chem. Geol.* **2008**, *249*, 1–35. [[CrossRef](#)]
86. Williams, I.S. U–Th–Pb geochronology by ion microprobe. *Rev. Econ. Geol.* **1998**, *7*, 1–35. [[CrossRef](#)]
87. Compston, W.; Williams, I.S.; Kirschvink, J.L.; Zichao, Z.; Guogan, M.A. Zircon U–Pb ages for the Early Cambrian time-scale. *J. Geol. Soc.* **1992**, *149*, 171–184. [[CrossRef](#)]
88. Paton, C.; Woodhead, J.D.; Hellstrom, J.C.; Hergt, J.M.; Greig, A.; Maas, R. Improved laser ablation U–Pb zircon geochronology through robust downhole fractionation correction. *Geochem. Geophys. Geosyst.* **2010**, *11*, Q0AA06. [[CrossRef](#)]
89. Ludwig, K.R. User’s Manual for Isoplot/Ex rev. 3.00: A Geochronological Toolkit for Microsoft Excel. *Berkeley Geochronol. Cent. Spec. Publ.* **2003**, *4*, 59.
90. Vervoort, J.D.; Patchett, P.J.; Söderlund, U.; Baker, M. Isotopic composition of Yb and the determination of Lu concentrations and Lu/Hf ratios by isotope dilution using MC–ICPMS. *Geochem. Geophys. Geosyst.* **2004**, *5*, Q11002. [[CrossRef](#)]
91. Blichert-Toft, J.; Albarède, F. The Lu–Hf isotope geochemistry of chondrites and the evolution of the mantle–crust system. *Earth Planet. Sci. Lett.* **1997**, *148*, 243–258. [[CrossRef](#)]
92. Griffin, W.L.; Pearson, N.J.; Belousova, E.; Jackson, S.E.; van Achenbergh, E.; O’Reilly, S.Y.; Shee, S.R. The Hf isotope composition of cratonic mantle: LAM–MC–ICPMS analysis of zircon megacrysts in kimberlites. *Geochim. Cosmochim. Acta* **2000**, *64*, 133–147. [[CrossRef](#)]
93. Liu, Y.S.; Zong, K.Q.; Kelemen, P.B.; Gao, S. Geochemistry and magmatic history of eclogites and ultramafic rocks from the Chinese continental scientific drill hole: Subduction and ultrahigh-pressure metamorphism of lower crustal cumulates. *Chem. Geol.* **2008**, *247*, 133–153. [[CrossRef](#)]
94. Lu, Y.F. GeoKit-A geochemical toolkit for Microsoft Excel. *Geochemical* **2004**, *5*, 459–464. (In Chinese with English abstract) [[CrossRef](#)]
95. Liang, X.R.; Wei, G.J.; Li, X.H.; Liu, Y. Precise measurement of <sup>143</sup>Nd/<sup>144</sup>Nd and Sm/Nd ratios using multiple-collectors inductively coupled plasma-mass spectrometer (MC–ICPMS). *Geochimica* **2003**, *1*, 91–96. (In Chinese with English abstract) [[CrossRef](#)]
96. Winchester, J.A.; Floyd, P.A. Geochemical discrimination of different magma series and their differentiation products using immobile elements. *Chem. Geol.* **1977**, *20*, 325–343. [[CrossRef](#)]
97. Pearce, J.A. Trace element characteristics of lavas from destructive plate boundaries. In *Andesites: Orogenic Andesites and Related Rocks*; Wiley & Sons: Hoboken, NJ, USA, 1982; pp. 525–548.
98. Sun, S.-s.; McDonough, W.F. Chemical and isotopic systematics of oceanic basalts: Implications for mantle composition and processes. *Geol. Soc. Lond. Spec. Publ.* **1989**, *42*, 313–345. [[CrossRef](#)]
99. Liu, H.C.; Wang, Y.J.; Cawood, P.A.; Fan, W.M.; Cai, Y.F.; Xing, X.W. Record of Tethyan ocean closure and Indosinian collision along the Ailaoshan suture zone (SW China). *Gondwana Res.* **2015**, *27*, 1292–1306. [[CrossRef](#)]
100. Liu, H.C.; Wang, Y.J.; Li, Z.H.; Zi, J.W.; Huangfu, P.P. Geodynamics of the Indosinian orogeny between the South China and Indochina blocks: Insights from latest Permian–Triassic granitoids and numerical modeling. *Geol. Soc. Am. Bull.* **2018**, *130*, 1289–1306. [[CrossRef](#)]
101. Leloup, P.H.; Lacassin, R.; Tapponnier, P.; Schärer, U.; Zhong, D.L.; Liu, X.H.; Zhang, L.S.; Ji, S.C.; Trinh, P.T. The Ailao Shan–Red River shear zone (Yunnan, China), Tertiary transform boundary of Indochina. *Tectonophysics* **1995**, *251*, 3–84. [[CrossRef](#)]
102. Nam, T.N. P–T–t paths and post-metamorphic exhumation of the Day Nui Con Voi shear zone in Vietnam. *Tectonophysics* **1998**, *290*, 299–318. [[CrossRef](#)]
103. Nakano, N.; Osanai, Y.; Owada, M.; Nam, T.N.; Charusiri, P.; Khamphavong, K. Tectonic evolution of high-grade metamorphic terranes in central Vietnam: Constraints from large-scale monazite geochronology. *J. Asian Earth Sci.* **2013**, *73*, 520–539. [[CrossRef](#)]

104. Lai, C.K. Tectonic Evolution of the Ailaoshan Fold Belt in Southwestern Yunnan, China. Ph.D. Thesis, University of Tasmania, Hobart, Australia, 2012.
105. Plank, T.; Langmuir, C.H. The chemical composition of subducting sediment and its consequences for the crust and mantle. *Chem. Geol.* **1998**, *145*, 325–394. [[CrossRef](#)]
106. Chauvel, C.; Lewin, E.; Carpentier, M.; Arndt, N.T.; Marini, J.C. Role of recycled oceanic basalt and sediment in generating the Hf–Nd mantle array. *Nat. Geosci.* **2008**, *1*, 64–67. [[CrossRef](#)]
107. La Flèche, M.R.; Camiré, G.; Jenner, G.A. Geochemistry of post-Acadian, Carboniferous continental intraplate basalts from the Maritimes Basin, Magdalen Islands, Québec, Canada. *Chem. Geol.* **1998**, *148*, 115–136. [[CrossRef](#)]
108. Xiao, L.; Xu, Y.G.; Mei, H.J.; Zheng, Y.F.; He, B.; Pirajno, F. Distinct mantle sources of low-Ti and high-Ti basalts from the western Emeishan large igneous province, SW China: Implications for plume–lithosphere interaction. *Earth Planet. Sci. Lett.* **2004**, *228*, 525–546. [[CrossRef](#)]
109. Su, Y.J. *Mid-Ocean Ridge Basalt Trace Element Systematics: Constraints from Database Management, ICPMS Analysis, Global Data Compilation, and Petrologic Modeling*; Columbia University: New York, NY, USA, 2003.
110. Vervoort, J.D.; Patchett, P.J.; Blichert-Toft, J.; Albarède, F. Relationships between Lu–Hf and Sm–Nd isotopic systems in the global sedimentary system. *Earth Planet. Sci. Lett.* **1999**, *168*, 79–99. [[CrossRef](#)]
111. Hu, W.J.; Zhong, H.; Zhu, W.G.; Bai, Z.J. Rift- and subduction-related crustal sequences in the Jinshajiang ophiolitic mélange, SW China: Insights into the eastern Paleo-Tethys. *Lithosphere* **2019**, *11*, 821–833. [[CrossRef](#)]
112. Xu, J.; Xia, X.P.; Lai, C.K.; Zhou, M.L.; Ma, P.F. First Identification of Late Permian Nb-Enriched Basalts in Ailaoshan Region (SW Yunnan, China): Contribution from Emeishan Plume to Subduction of Eastern Paleotethys. *Geophys. Res. Lett.* **2019**, *46*, 2511–2523. [[CrossRef](#)]
113. Xu, W.T.; Liu, F.L.; Ji, L.; Xu, W. Geochemistry, geochronology and geological implication of amphibolites in Ailao Shan-Day Nui Con Voi metamorphic complex belt, southeastern Tibetan Plateau. *Acta Petrol. Sin.* **2020**, *36*, 3622–3645. (In Chinese with English abstract) [[CrossRef](#)]
114. Xu, W.T.; Liu, F.L. The Late Paleozoic arc-back arc system in western Ailaoshan: Evidence from geochemistry and geochronology of basic rocks. *Acta Petrol. Mineral.* **2020**, *39*, 406–422. (In Chinese with English abstract)
115. Wang, B.D.; Wang, L.Q.; Chen, J.L.; Yin, F.G.; Wang, D.B.; Zhang, W.P.; Chen, L.K.; Liu, H. Triassic three-stage collision in the Paleo-Tethys: Constraints from magmatism in the Jiangda–Deqen–Weixi continental margin arc, SW China. *Gondwana Res.* **2014**, *26*, 475–491. [[CrossRef](#)]
116. Pearce, J.A.; Norry, M.J. Petrogenetic implications of Ti–Zr–Y and Nb variations in volcanic rocks. *Contrib. Mineral. Petrol.* **1979**, *69*, 33–47. [[CrossRef](#)]
117. Xu, J.; Xia, X.P.; Cai, K.D.; Lai, C.K.; Liu, X.J.; Yang, Q.; Zhou, M.L.; Ma, P.F.; Zhang, L. Remnants of a Middle Triassic island arc on western margin of South China Block: Evidence for bipolar subduction of the Paleotethyan Ailaoshan Ocean. *Lithos* **2020**, *360–361*, 105447. [[CrossRef](#)]
118. Patiño Douce, A.E. What do experiments tell us about the relative contributions of crust and mantle to the origin of granitic magmas? *Geol. Soc. Lond. Spec. Publ.* **1999**, *168*, 55–75. [[CrossRef](#)]
119. Rapp, R.P.; Watson, E.B. Dehydration Melting of Metabasalt at 8–32 kbar: Implications for Continental Growth and Crust–Mantle Recycling. *J. Petrol.* **1995**, *36*, 891–931. [[CrossRef](#)]
120. Wu, F.Y.; Li, X.H.; Zheng, Y.F.; Gao, S. Lu–Hf isotopic systematics and their applications in petrology. *Acta Petrol. Sin.* **2007**, *23*, 185–220. (In Chinese with English abstract)
121. Davies, J.H.; Friedhelm, v.B. Slab breakoff: A model of lithosphere detachment and its test in the magmatism and deformation of collisional orogens. *Earth Planet. Sci. Lett.* **1995**, *129*, 85–102. [[CrossRef](#)]
122. Kay, R.W.; Mahlburg Kay, S. Delamination and delamination magmatism. *Tectonophysics* **1993**, *219*, 177–189. [[CrossRef](#)]
123. Wu, S.Y.; Hou, L.; Jowitt, S.M.; Ding, J.; Zhang, J.-R.; Zhu, S.B.; Zhao, Z.Y. Geochronology, geochemistry and petrogenesis of Late Triassic dolerites associated with the Nibao gold deposit, Youjiang Basin, southwestern China: Implications for post-collisional magmatism and its relationships with Carlin-like gold mineralization. *Ore Geol. Rev.* **2019**, *111*, 102971. [[CrossRef](#)]
124. Wu, S.Y.; Hou, L.; Ding, J.; Zhang, J.R.; Zhu, S.B. Deep magma evolution in the extensional Youjiang Basin in late Yanshanian period: Evidence from geochemical characteristics of Baiceng ultramafic rock, Guizhou Province. *Geol. Bull. China* **2017**, *36*, 445–458, (In Chinese with English abstract).
125. Mo, X.X.; Shen, S.Y.; Zhu, Q.W. *Volcanics-Ophiolites and Related Mineralization in the Middle Southern Segment of Sanjiang Region*; Beijing Geology Publications House: Beijing, China, 1998; pp. 1–128. (In Chinese)
126. Wu, F.Y.; Wang, B.; Zhao, L.; Xiao, W.J.; Zhu, R.X. Tethyan geodynamics. *Acta Petrol. Sin.* **2020**, *36*, 1627–1674. (In Chinese with English abstract) [[CrossRef](#)]
127. He, W.Y.; Yang, L.Q.; Lu, Y.J.; Jeon, H.; Xie, S.X.; Gao, X. Zircon U–Pb dating, geochemistry and Sr–Nd–Hf–O isotopes for the Baimaxueshan granodiorites and mafic microgranulars enclaves in the Sanjiang Orogen: Evidence for westward subduction of Paleo-Tethys. *Gondwana Res.* **2018**, *62*, 112–126. [[CrossRef](#)]

128. Xia, X.P.; Xu, J.; Huang, C.; Long, X.P.; Zhou, M.L. Subduction polarity of the Ailaoshan Ocean (eastern Paleotethys): Constraints from detrital zircon U-Pb and Hf-O isotopes for the Longtan Formation. *Geol. Soc. Am. Bull.* **2019**, *132*, 987–996. [[CrossRef](#)]
129. Xu, J.; Xia, X.P.; Wang, Q.; Spencer, C.J.; He, B.; Lai, C.K. Low- $\delta^{18}\text{O}$  A-type granites in SW China: Evidence for the interaction between the subducted Paleotethyan slab and the Emeishan mantle plume. *GSA Bull.* **2021**, *134*, 81–93. [[CrossRef](#)]
130. Wu, S.Y.; Hou, L.; Ding, J.; Wu, W.; Qin, K.; Zhang, J.R.; Zhu, S.B. Ore-controlling structure types and characteristics of ore-forming fluid of the Carlin-type gold orefield in southwestern Guizhou, China. *Acta Petrol. Sin.* **2016**, *32*, 2407–2424. (In Chinese with English abstract)
131. Xu, W.; Liu, F.L.; Dong, Y.S. Cambrian to Triassic geodynamic evolution of central Qiangtang, Tibet. *Earth-Sci. Rev.* **2020**, *201*, 103083. [[CrossRef](#)]